Systems/Circuits

# Parvalbumin$^+$ and Npas1$^+$ Pallidal Neurons Have Distinct Circuit Topology and Function

Arin Pamukcu,[1] Qiaoling Cui,[1] Harry S. Xenias,[1] Brianna L. Berceau,[1] Elizabeth C. Augustine,[1] Isabel Fan,[1] Saivasudha Chalasani,[1] Adam W. Hantman,[2] Talia N. Lerner,[1] Simina M. Boca,[3] and C. Savio Chan[1]

[1]Department of Physiology, Feinberg School of Medicine, Northwestern University, Chicago, Illinois 60611, [2]Janelia Research Campus, Howard Hughes Medical Institute, Ashburn, Virginia 20147, and [3]Innovation Center for Biomedical Informatics, Georgetown University Medical Center, Washington, DC 20007

The external globus pallidus (GPe) is a critical node within the basal ganglia circuit. Phasic changes in the activity of GPe neurons during movement and their alterations in Parkinson's disease (PD) argue that the GPe is important in motor control. Parvalbumin-positive (PV$^+$) neurons and Npas1$^+$ neurons are the two principal neuron classes in the GPe. The distinct electrophysiological properties and axonal projection patterns argue that these two neuron classes serve different roles in regulating motor output. However, the causal relationship between GPe neuron classes and movement remains to be established. Here, by using optogenetic approaches in mice (both males and females), we showed that PV$^+$ neurons and Npas1$^+$ neurons promoted and suppressed locomotion, respectively. Moreover, PV$^+$ neurons and Npas1$^+$ neurons are under different synaptic influences from the subthalamic nucleus (STN). Additionally, we found a selective weakening of STN inputs to PV$^+$ neurons in the chronic 6-hydroxydopamine lesion model of PD. This finding reinforces the idea that the reciprocally connected GPe–STN network plays a key role in disease symptomatology and thus provides the basis for future circuit-based therapies.

*Key words:* 6-OHDA; basal ganglia; globus pallidus; motor control; Parkinson's disease; subthalamic nucleus

---

**Significance Statement**

The external pallidum is a key, yet an understudied component of the basal ganglia. Neural activity in the pallidum goes awry in neurologic diseases, such as Parkinson's disease. While this strongly argues that the pallidum plays a critical role in motor control, it has been difficult to establish the causal relationship between pallidal activity and motor function/dysfunction. This was in part because of the cellular complexity of the pallidum. Here, we showed that the two principal neuron types in the pallidum have opposing roles in motor control. In addition, we described the differences in their synaptic influence. Importantly, our research provides new insights into the cellular and circuit mechanisms that explain the hypokinetic features of Parkinson's disease.

---

## Introduction

The basal ganglia are involved in motor control and adaptive behavior (Mink and Thach, 1991b; DeLong and Wichmann, 2007; Graybiel, 2008; Pennartz et al., 2009; Redgrave et al., 2010; Ito and Doya, 2011; Nambu and Tachibana, 2014; Jahanshahi et al., 2015; Dudman and Krakauer, 2016; Mink, 2018; Cox and Witten, 2019; Klaus et al., 2019). By providing a wide projection to all structures within the basal ganglia, the external globus pallidus (GPe) is theorized to critically influence information processing within this macrocircuit (Albin et al., 1989, 1995; DeLong, 1990; Parent and Hazrati, 1995; Mink, 1996; Bergman et al., 1998; Smith et al., 1998; DeLong and Wichmann, 2007; Kita, 2007; Hegeman et al., 2016; Crompe et al., 2020). Because of the complexity in cellular composition and axonal projection patterns (Sato et al., 2000b; Mastro et al., 2014; Abdi et al., 2015; Dodson et al., 2015; Hernández et

al., 2015; Fujiyama et al., 2016; Saunders et al., 2016, 2018; Abecassis et al., 2020), it has been challenging to demonstrate the causal roles of the GPe in motor control.

We and others established that the GPe contains two principal neuron classes distinguished by their expression of the calcium-binding protein parvalbumin (PV) or the transcription factor Npas1. They account for ~50% and 30% of the GPe neuron population, respectively (Flandin et al., 2010; Nóbrega-Pereira et al., 2010; Abdi et al., 2015; Dodson et al., 2015; Hernández et al., 2015; Hegeman et al., 2016; Abecassis et al., 2020). $PV^+$ neurons and $Npas1^+$ neurons have different firing characteristics and projection targets. Specifically, $PV^+$ neurons exhibit higher firing rates and preferentially target the subthalamic nucleus (STN) and substantia nigra pars reticulata (SNr), whereas $Npas1^+$ neurons have lower firing rates and preferentially target the dorsal striatum (dStr) (Abdi et al., 2015; Hernández et al., 2015; Saunders et al., 2016; Mastro et al., 2017; Abecassis et al., 2020; Cherian et al., 2020). These results suggest that $PV^+$ neurons and $Npas1^+$ neurons likely play unique functional roles. Though this concept is fundamental to the organization and operating principles of the basal ganglia, no direct evidence has been presented.

To fill this critical knowledge gap, here we used contemporary circuit tools to examine the functional roles and synaptic inputs of GPe neuron subpopulations in mice. In accordance with their distinct electrophysiological and circuit characteristics, we found that $PV^+$ neurons and $Npas1^+$ neurons have distinct functional roles—$PV^+$ neurons promote locomotion and $Npas1^+$ neurons suppress it. By examining the excitatory inputs to the GPe, we showed that STN input to the GPe is unique in its cell type specificity and preferentially targets $PV^+$ neurons over $Npas1^+$ neurons. Abnormal activity in the STN–GPe network has been postulated to underlie the hypokinetic symptoms of Parkinson's disease (PD); however, the cell and circuit basis for its emergence remain poorly understood. By harnessing a chronic unilateral 6-hydroxydopamine (6-OHDA) lesion model of PD, we showed that the STN–$PV^+$ input is selectively weakened in the chronic 6-OHDA-lesioned model of PD. In vivo optogenetic stimulation of $PV^+$ neurons promoted locomotion and alleviated hypokinetic symptoms in 6-OHDA-lesioned mice. These results demonstrate the causal role of $PV^+$ neurons in PD symptomatology, thus providing the basis for circuit manipulations in treatments of PD.

## Materials and Methods

*Mice.* All procedures were performed in accordance with protocols approved by Northwestern University Institutional Animal Care and Use Committees and were in compliance with the National Institutes of Health *Guide to the Care and Use of Laboratory Animals*. Experiments were conducted with the following mouse lines: A2a-Cre [Adora2a-Cre BAC; stock #031168, Mutant Mouse Regional Resource Center (MMRRC)]; C57BL/6J (stock #000664, The Jackson Laboratory); D1-Cre (Drd1a-Cre BAC; stock #029178, MMRRC); D2-eGFP (Drd2-eGFP BAC; stock #000230, MMRRC); Lox-STOP-Lox(LSL)-tdTom (Ai14; stock #007914, The Jackson Laboratory); Npas1-Cre-tdTom (Npas1-Cre-tdTomato BAC; stock #027718, The Jackson Laboratory); PV-Cre (PV-ires-Cre; stock #017320, The Jackson Laboratory); and PV-tdTom (PV-tdTomato BAC; stock #027395, The Jackson Laboratory). The Npas1-Cre-tdTom BAC mouse was generated in-house (Hernández et al., 2015). PV-Cre was crossed with LSL-tdTom to generate PV-L-tdTom (PV-Cre;LSL-tdTom; Abecassis et al., 2020). Only heterozygous and hemizygous mice were used throughout the study to minimize the potential alteration of the phenotypes in mice carrying the transgene alleles (Chan et al., 2012). Mice were group housed in a 12 h light/dark

**Table 1. Detailed information on viral injections**

| Viral vector | Source | Working titer (viral genome/ml) |
|---|---|---|
| AAV₉.EF1a.DIO. hChR2(H134R).eYFP | Addgene, catalog #20298 | 5.55E + 12 (GPe) |
| | | 2.00E + 12 (STN) |
| | | 2.20E + 12 (dStr) |
| AAV₉.EF1a.DIO.eYFP | Virovek | 5.55E + 12 |
| AAV₁.CKIIa.stGtACR2.FusionRed | Addgene, catalog #105669 | 3.00E + 11 |
| AAV₁.hSyn1.SIO.stGtACR2.FusionRed | Addgene, catalog #105677 | 5.00E + 11 |
| AAV₉.Syn.ChR2(H134R).eYFP | Addgene, catalog #26973P | 2.68E + 12 |
| AAVretro.Syn.Cre | Janelia | 2.30E + 11 |

cycle. Food and water were provided *ad libitum*. All mouse lines were maintained by backcrossing with C57BL/6J stock. The genotypes of all transgenic mice were determined by tail biopsy followed by PCR to identify the presence of the relevant transgenes. Both male and female mice were used in this study.

*Stereotaxic injections.* Mice aged postnatal day 30–35 were anesthetized in an isoflurane induction chamber at 3–4% isoflurane and immobilized on a stereotaxic frame (David Kopf Instruments). Anesthesia was maintained using 1–2% isoflurane. The scalp was opened using a scalpel and a small craniotomy (diameter, 1 mm) was made with a dental drill (Osada). Adeno-associated viruses (AAVs) were infused with calibrated 5 µl glass pipettes (VWR) pulled to have a tip diameter of 3 µm. The injection needle was left *in situ* for 5–10 min following the end of the injection to maximize the tissue retention of AAV and decrease capillary spread on pipette withdrawal. Experiments were performed 4–6 weeks after stereotaxic surgeries. The locations of the targeted injections were visually inspected under epifluorescence microscopy in *ex vivo* slices or histologically verified *post hoc*.

For *in vivo* channelrhodopsin-2 (ChR2) stimulation of $PV^+$ neurons or $Npas1^+$ neurons, 90 nl of AAV₉.EF1a.DIO.hChR2(H134R).eYFP. WRE was injected into the GPe of PV-Cre or Npas1-Cre-tdTom mice. Alternatively, AAV₉.EF1a.DIO.eYFP.WPRE was injected into the GPe as a viral control. For *in vivo Guillardia theta* anion channelrhodopsin-2 (GtACR2) inhibition of the GPe, 90 nl of AAV₁.hSyn1.SIO.stGtACR2. FusionRed was injected into the GPe of PV-Cre or Npas1-Cre-tdTom mice. For *in vivo* GtACR2 inhibition of the STN, 45 nl of AAV₁.CKIIa. stGtACR2.FusionRed was injected into the STN. For *in vivo* ChR2 stimulation of direct-pathway spiny projection neurons (dSPNs) and indirect-pathway SPNs (iSPNs), 720 nl of AAV₉.EF1a.DIO.hChR2(H134R). eYFP.WRE was injected into the dStr of D1-Cre and A2a-Cre mice, respectively. All surgeries for *in vivo* experiments were performed bilaterally.

To explore STN-specific ChR2 expression via retrograde Cre delivery, transduction patterns of AAVretro.Cre were first examined in LSL-tdTom mice; 90 nl of AAVretro.Cre was injected into the SNr. For Cre recombinase-inducible expression (CreOn) of ChR2 in the STN, 90 nl of AAVretro.Cre was injected into the SNr of the C57BL/6J mice, and 45 nl of AAV₉.EF1a.DIO.ChR2(H134R).eYFP into the STN. For *ex vivo* electrophysiological recordings of STN inputs, 45 nl of AAV₉.Syn.ChR2 (H134R).eYFP was injected into the STN. For recordings of pedunculopontine nucleus (PPN) and parafascicular nucleus of the thalamus (PF Thal) glutamatergic inputs, 90 nl of AAV₉.Syn.ChR2(H134R).eYFP was injected. A full listing of the viral constructs and titer information is available in Table 1. Injection coordinates are specified in Table 2.

*Fiber implantations and behavioral testing.* Three weeks after stereotaxic injections, fiber-optic cannulae were implanted bilaterally at the region of interest (Table 3). Each fiber cannula was assembled with an optical fiber [0.66 numerical aperture (NA), 250 µm core; Prizmatix] secured into a zirconia ferrule (outer diameter, 1.25 mm; Prizmatix) with nonfluorescent epoxy (Thorlabs). To determine the intensity of light exiting fibers, the output of fibers was measured with a power meter (Thorlabs). Cannulae were fixed to the skull using dental cement (Parkell). Mice were allowed to recover for 1–2 weeks before behavioral testing.

Behavioral tests were performed in a standard lit room between 2:00 and 7:00 P.M. *In vivo* optogenetic experiments were performed in an

**Table 2. Viral and 6-OHDA injection coordinates**

| Region | Volume per hemisphere (μl) | Rostral to bregma (mm) | Lateral to bregma (mm) | Ventral to the skull (mm) |
|---|---|---|---|---|
| GPe | 90 | −0.28 | 2.10 | 4.00 |
| STN | 45 | −1.70 | 1.60 | 4.50 |
| SNr | 90 | −3.00 | 1.60 | 4.20 |
| dStr | 720 | 0.90 | 1.40 | 3.20, 3.60 |
| PPN | 90 | −4.50 | 1.25 | 3.50 |
| PF Thal | 90 | −2.22 | 0.64 | 3.20 |
| MFB | 990 | −0.70 | 1.10 | 4.95 |

MFB, Medial forebrain bundle.

**Table 3. Implantation coordinates**

| Region | Rostral to bregma (mm) | Lateral to bregma (mm) | Ventral to the skull (mm) |
|---|---|---|---|
| GPe | −0.28 | 2.1 | 3.8 |
| STN | −1.70 | 1.6 | 4.3 |
| SNr | −3.00 | 1.6 | 4.1 |
| dStr | 0.90 | 1.4 | 3.0 |

opaque white plastic open-field box (28 × 28 cm), which was cleaned with 70% ethanol. On the day before optogenetic experiments, each mouse was allowed to acclimate to the open-field box for 20 min, with a fiber-optic cable attached to the implant via a rotary joint (Prizmatix). Pretrial, basal ambulatory activity was collected for 5 min at the beginning of the behavioral session. For ChR2 activation, mice were subjected to either a single, sustained light pulse or a patterned pulse train (5 ms pulses at 20 Hz) delivered for 10 s. For GtACR2 activation, only the sustained protocol was used. A blue (peak, ~455 nm) LED (Prizmatix) was used to activate both opsins. The light power used for opsin activation was 12–18 mW measured at the fiber tip. Up to 10 trials were run for any given protocol with a 1 min intertrial interval. Movement data were collected with an overhead camera at the maximum sampling rate (10 Hz). Mouse position was tracked using EthoVision XT (Noldus). After the completion of behavioral experiments, transgene expression patterns and fiber-optic implant locations were histologically verified *post hoc*. Only histologically validated subjects were included in this study.

Speed of locomotion was computed from the distance traveled within the open-field arena per unit time. "Light-period" corresponds to 10 s of light delivery. "Pre-period" and "post-period" correspond to the 10 s epoch before and after light delivery, respectively. The fold change in locomotor activity was calculated by dividing the difference in speed between light-period and pre-period by that of pre-period. Immobility was defined as periods with horizontal displacement ≤1 cm/s for at least 0.1 s. Mobility bouts were defined as periods with horizontal displacement >1 cm/s for at least 0.1 s. To calculate normalized speed, data for each trial were divided by the mean spontaneous locomotor activity measured from 25 s immediately before the light-period. The median differences in movement speed between pre-period and light-period and their 95% confidence intervals were estimated (https://www.estimationstats.com), 5000 bootstrap samples were taken, bias was corrected, and accelerated corrections were applied to the resampling bootstrap distributions to adjust for both bias and the skewness (Ho et al., 2019). Logistic regressions were performed using R codes implemented in JASP (https://jasp-stats.org/). For single-trial analyses, data from both patterned and sustained stimuli were pooled. We considered logistic regressions for outcomes representing changes in speed during pre-period and light-period above the 0.1-, 1-, and 10-fold cutoffs for PV-Cre mice, or below the 0.1-, 0.5-, and 0.8-fold cutoffs for Npas1-Cre-tdTom mice, with each regression having the strain and manipulation condition as the explanatory variable. Speed during pre-period was considered as a covariate. To examine whether there was hysteresis associated with optogenetic stimulation, trial number was considered as a factor in the model.

*Chronic 6-hydroxydopamine lesion.* To study the changes in the STN–GPe network in a parkinsonian state, a chronic, unilateral 6-hydroxydopmaine (6-OHDA) lesion model of PD was used to achieve a loss of dopamine neurons of the nigrostriatal system (Ungerstedt, 1968; Beal, 2001; Dauer and Przedborski, 2003; Meredith and Kang, 2006; Bezard and Przedborski, 2011). Unilateral 6-OHDA lesioning was performed using standard procedures (Chan et al., 2011, 2012; Hernández et al., 2015; Cui et al., 2016; Glajch et al., 2016). In brief, 6-OHDA (2.5 μg/μl dissolved in 0.9% w/v NaCl with 0.1% w/v ascorbic acid) was injected into the medial forebrain bundle (Table 2) of the left hemisphere. Three weeks after the 6-OHDA injection, lesion success was determined by performing the cylinder test to assess forelimb use impairments (Schallert et al., 2000; Iancu et al., 2005; Chan et al., 2011; Cui et al., 2016). The ratio of ipsilateral to total forepaw touches was used to determine the success of the lesion. In this task, during a 5 min exploratory behavioral assessment in a clear glass cylinder, weight-bearing contacts made by each forepaw on the glass walls of the cylinder were manually quantified. Forelimb use asymmetry was determined by calculating left, right, and combined forepaw touches. As impairment of the contralateral (i.e., right) forepaw was expected with 6-OHDA lesions, a higher ratio of left to the sum of all touches indicates a more severe lesion. A ratio of 1.0 indicates that the mice only used the left forelimb (ipsilateral to the lesion) for the entire test session. Mice with a forepaw/touch ratio of <0.6 were considered poorly lesioned and were excluded from the study.

Ex vivo *electrophysiological recordings.* Mice aged postnatal day 60–90 (4–6 weeks after AAV and 6-OHDA injections) were anesthetized with a ketamine-xylazine mixture and perfused transcardially with ice-cold artificial CSF (aCSF) containing the following (in mM): 125 NaCl, 2.5 KCl, 1.25 NaH$_2$PO$_4$, 2.0 CaCl$_2$, 1.0 MgCl$_2$, 25 NaHCO$_3$, and 12.5 glucose, bubbled continuously with carbogen (95% O$_2$ and 5% CO$_2$). The brains were rapidly removed, glued to the stage of a vibrating microtome (Leica Instruments), and immersed in ice-cold aCSF. Parasagittal slices containing the GPe were cut at a thickness of 240 μm and transferred to a holding chamber, where they were submerged in aCSF with 3.33 mM pyruvate and 0.07 mM L-glutathione at 37°C for 30 min, and brought to room temperature before recording. Slices were then transferred to a small volume (0.5 ml) Delrin recording chamber that was mounted on a fixed-stage, upright microscope (Olympus). As there is no clear demarcation between the GPe and the more ventral structures in *ex vivo* brain slices, only neurons in the dorsal two-thirds of the GPe were sampled for electrophysiological analyses. GPe neurons were visualized using differential interference contrast optics, illuminated at 735 nm (Thorlabs), and imaged with a 60× 1.0 NA water-immersion objective (Olympus) and a CCD camera (QImaging). Genetically labeled GPe neurons were identified based on their somatic tdTomato fluorescence and examined with epifluorescence microscopy using a white (6500 K) LED (Thorlabs) and an appropriate filter cube (Semrock). Targeting of ChR2-eYFP (enhanced yellow fluorescent protein) was assessed by inspecting eYFP fluorescence before each recording. Mice with viral spread beyond STN and zona incerta (ZI) were excluded from further experimentation.

Recordings were made at room temperature (20–22°C) with patch electrodes fabricated from capillary glass (Sutter Instruments) pulled on a Flaming-Brown puller (Sutter Instruments) and fire polished with a microforge (Narishige) immediately before use. Pipette resistance was typically 2–4 MΩ. The internal solution for cell-attached and voltage-clamp recordings consisted of the following (in mM): 125 CsMeSO$_3$, 10 Na$_2$-phosphocreatine, 5 tetraethylammonium chloride, 5 QX-314 Cl, 5 HEPES-K, 5 EGTA-K, 2 Mg$_2$ATP, 0.5 CaCl$_2$, 0.5 Na$_3$GTP, and 0.2% w/v biocytin, with pH adjusted to 7.25–7.30 with CsOH. SR95531 (10 μM) and CGP55845A (1 μM) were included in the bath during recordings to block GABAergic transmission. For SPN recordings, Alexa Fluor 594 hydrazide (10–20 μM; Thermo Fisher Scientific) was included in the pipette solution to confirm the identity by visualizing the presence of spine-dense dendrites. Somatic patch-clamp recordings were obtained with an amplifier (Molecular Devices). The signal for all voltage-clamp recordings was filtered at 1 kHz and digitized at 10 kHz with a digitizer (Molecular Devices). For voltage-clamp recordings, series resistance was measured but not compensated for.
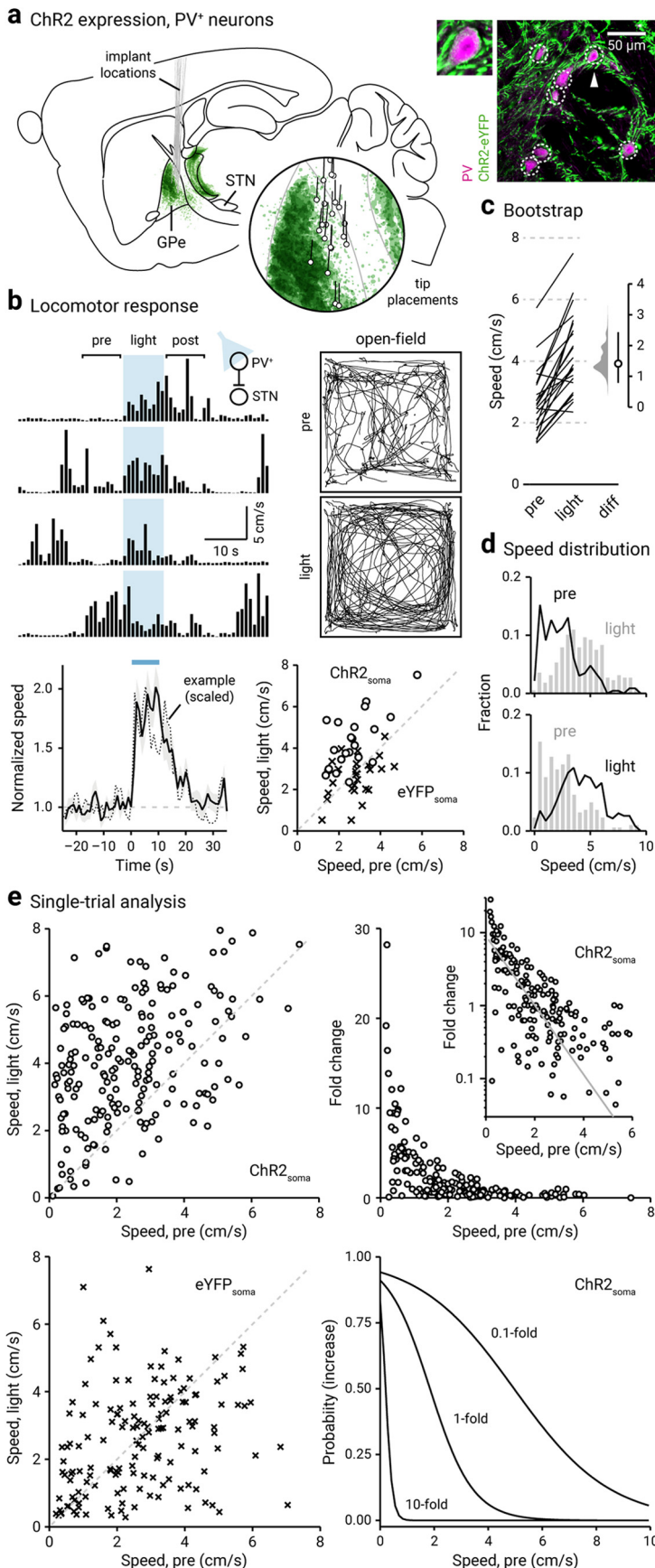
**Figure 1.** Optogenetic stimulation of PV$^+$ neurons promotes locomotion. **a**, Left, Representation of ChR2-eYFP expression patterns and fiber-optic implant locations in PV-Cre mice ($n = 12$). Inset, Representation of optical fiber tip placements in relation to the GPe and neighboring structures. Right, Confocal micrographs showing the cellular

The data were discarded if series resistance increased by 20% during recordings. Stimulus generation and data acquisition were performed using pClamp (Molecular Devices).

To measure the spontaneous and driven firing of GPe neurons, the cell-attached configuration was used to prevent the disruption of intracellular milieu. The average spontaneous firing was measured after 2 min of stable firing. To measure the driven firing of GPe neurons, input from the STN was optogenetically stimulated with 2 ms pulses at 10 Hz for 2 s. The average firing rate during the 2 s stimulation period was taken as the driven firing rates of the respective cells. Whole-cell voltage-clamp recordings were used to measure EPSCs. GPe neurons were voltage clamped at –50 mV; terminals from excitatory inputs (from STN, PPN, and PF Thal) synapsed within the GPe were optogenetically stimulated for 2 ms. For *ex vivo* optogenetic experiments, blue excitation wavelength (peak, ~450 nm) from two daylight (6500 K) LEDs (Thorlabs) was delivered to the tissue slice from both a 60× water-immersion objective and a 0.9 NA air condenser with the aid of 520 nm dichroic beamsplitters (Semrock). Light delivery was made at the site of electrophysiological recordings with a field of illumination of ~500 μm in diameter. To measure STN input without the topographical biasing of the STN axons in the GPe, recordings were made from neighboring tdTomato$^+$ and tdTomato$^-$ neurons (<150 μm

←

specificity of ChR2-eYFP expression in the GPe. For clarity, a magnified example (arrowhead) is shown. **b**, Top, left, A representative example of the locomotor activity of a single mouse across four trials. The schematic diagram shows the site of light delivery. Blue shaded area indicates the duration (10 s) of light delivery. Top, right, Movement tracks corresponding to the pre-period (top) and light-period (bottom). Six representative mice (10 trials from each) are presented. Bottom, left, A plot showing the relationship between normalized speed and time. Blue bar indicates the duration (10 s) of light delivery. The dotted horizontal line indicates the baseline locomotor activity level. Black solid trace is the population mean calculated from all mice; shading indicates the SEM. Black dotted trace is a representative example from a single mouse; data were scaled to facilitate comparison. Bottom, right, Speed during light-period against speed during pre-period is plotted. Data from PV-Cre mice expressing ChR2-eYFP (circles) and eYFP (crosses) are displayed. Each marker represents a mouse. The diagonal line indicates unity (i.e., $x = y$). Data points for ChR2-eYFP are systematically shifted upward relative to unity. **c**, Slopegraph showing the response of each mouse on optogenetic stimulation of PV$^+$ neurons. The slope of each line shows the magnitude and direction of change. Median difference is plotted on a floating axis. The smoothed density represents bootstrap resampled data. The median difference is indicated as a circle, and the 95% confidence interval is indicated by the length of vertical lines. **d**, Speed distributions of mice during pre-period and light-period are shown. **e**, Top, left, A scatter plot showing the pairwise relationship between speed during light-period and speed during pre-period from PV-Cre mice expressing ChR2-eYFP. Each marker is a trial. The diagonal line indicates unity. Top right, Fold change in speed with light delivery against speed during pre-period from PV-Cre mice expressing ChR2-eYFP. Each marker is a trial. Inset, Same data displayed with fold increase on a log scale. Grayline is a monoexponential fit of the data. Bottom, left, A plot showing the speed during light-period versus speed during pre-period. Data from PV-Cre mice expressing eYFP are displayed. Each marker is a trial. The diagonal line indicates unity. Bottom, right, Probability of increase against speed during pre-period. Logistic regression curves fitted to data for 0.1-fold, 1-fold, and 10-fold increases are displayed.

apart) in both PV-L-tdTom and Npas1-Cre-tdTom mice. To study STN input with CreOn expression of ChR2, EPSC recordings were made from tdTomato$^+$ and tdTomato$^-$ GPe neurons in PV-L-tdTom mice. Corticostriatal EPSCs were evoked with electrical stimulation using parallel bipolar tungsten electrodes (Frederick Haer) placed in the cortex. To measure AMPA and NMDA receptor-mediated currents, the holding potential of recorded neurons was alternated between –80 and +40 mV. AMPA receptor-dependent currents were measured from the peak amplitude of EPSCs at –80 mV. NMDA receptor-dependent currents were measured at 50 ms after the EPSC peak at +40 mV. The AMPA-NMDA ratio was calculated by dividing the AMPA current by the NMDA current.

*Histology.* For histologic verification of injection and implantation sites in mice used for *in vivo* behavioral experiments, mice were anesthetized deeply with a ketamine-xylazine mixture and perfused transcardially first with 0.01 M PBS followed by a fixative containing 4% paraformaldehyde (PFA), pH 7.4. Brain tissue was then postfixed in the same fixative for 2 h at 4°C. Tissue blocks containing the GPe were sectioned sagittally using a vibrating microtome (Leica Instruments) at a thickness of 60 μm. Sections were then washed, mounted, and coverslipped. Standard immunohistological procedures (Abecassis et al., 2020) were performed in a subset of brain tissues to validate the cellular specificity of transgene expression. Sections were imaged under an epifluorescence microscope (Keyence), and each section was visually inspected. Graphical representations were created using a thresholding based protocol in Fiji (http://fiji.sc/Fiji; Schindelin et al., 2012), where regions of interest were selected to show transgene expression in the primary injection sites. For histologic verification of AAV$_{retro}$-mediated recombination and the quantification of STN fibers, images were taken on a laser-scanning confocal microscope with a 10× 0.45 NA air objective and a 60× 1.35 NA oil-immersion objective (Olympus).

To quantify STN axonal fibers in the GPe, identical histologic procedures were used. Sections were imaged on a laser-scanning confocal microscope with a 10× 0.45 NA air objective (Olympus). Values for "area," "area fraction," and "integrated density" were quantified using Fiji. Specifically, area represents the user-defined area of the GPe in a sagittal section, and area fraction represents the fraction of area that contains pixels with values above the set threshold, in this case, pixels with eYFP-labeled STN fibers. Integrated density represents the sum of all pixels within the selected area (i.e., the sum of absolute pixel values), which was used as a measure of the density of STN fibers within the GPe. To quantify putative STN terminals within the GPe, standard immunohistological procedures were performed. Floating tissue sections were reacted with antibodies for GFP (1:1000; Abcam) and VGluT2 (1:1000; NeuroMab). Images were taken on a laser-scanning confocal microscope with a 60× 1.35 NA oil-immersion objective and 2× digital zoom. Three nonoverlapping fields (106.7 × 106.7 μm$^2$) were imaged from each section; 5 μm serial optical sections (z-stacks, at 1 μm intervals) were acquired. Puncta were deemed bona fide STN–GPe synaptic boutons only if they showed spatial overlap of eYFP and VGluT2 signals across all three orthogonal planes. GPe sections from three different equally spaced (400 μm) lateromedial levels were sampled (Hernández et al., 2015; Abecassis et al., 2020) from the left hemisphere.

Brain tissue used for *ex vivo* electrophysiological recordings was stored in 4% PFA for 24 h. PFA-fixed tissues were mounted on microscope slides, coverslipped with Prolong Gold antifade mounting medium (Thermo Fisher Scientific), and imaged under an epifluorescence microscope (Keyence) to inspect the fluorescent signal from the site of viral injection.

*Experimental design and statistical analyses.* Statistical analyses were performed with MATLAB (MathWorks) and Prism (GraphPad Software). Custom analysis codes are available on GitHub (https://github.com/chanlab). The sample size (n value) shown represents the number of mice for *in vivo* behavior experiments and the number of cells for *ex vivo* electrophysiological experiments. Unless noted otherwise, data are presented as median values ± median absolute deviations (MADs; Leys et al., 2013) as measures of central tendency and statistical dispersion, respectively. Box plots are used for graphical representation of the distribution of values (Krzywinski and Altman, 2014; Streit and



**Movie 1.** *In vivo* optogenetic stimulation of PV$^+$ neurons promoted locomotion. Representative movie of a mouse in an open field arena showing increased locomotion upon optogenetic stimulation of PV$^+$ neurons. Behavior from two consecutive trials is shown. Video is shown at 2× speed. [View online]

Gehlenborg, 2014; Nuzzo, 2016). In a box plot, the central line represents the median, the box edges represent the interquartile ranges, and whiskers represent 10th to 90th percentiles. No statistical method was used to predetermine sample sizes. Comparisons for unpaired samples were performed using a Mann–Whitney $U$ test. Comparisons for paired samples were performed using the Wilcoxon signed-rank test. The Fisher's exact test was used to determine whether there were nonrandom associations in two nominal variables with a threshold ($\alpha$) of 0.05 for significance. Statistical significance was set at $p < 0.05$. Unless <0.0001 or >0.99, exact $p$ values (two tailed) are reported. No multiple testing corrections were considered.

## Results

We sought to dissect the relationship between GPe neuron activity and motor output with cell type-specific strategies. To confer transgene expression specificity in PV$^+$ neurons and Npas1$^+$ neurons, we used CreOn AAVs in conjunction with PV-Cre and Npas1-Cre-tdTom mouse lines, respectively. *In vivo* optogenetics, which provides a relatively high temporal resolution, was used to interrogate the roles that PV$^+$ neurons and Npas1$^+$ neurons play in regulating full-body movements—locomotion. Locomotor activity of mice in an open-field arena across individual trials was analyzed. We focused on the following three defined time windows relative to light delivery: the pre-period (pre; −10 to 0 s), the light-period (light; 0–10 s), and the post-period (post; 10–20 s).

### PV$^+$ neurons promote movement

Stimulation of PV$^+$ neurons *in vivo* using ChR2 (an excitatory opsin; Boyden et al., 2005; Fig. 1a) induced an increase in motor output, as measured by the duration of movement periods (data not shown) and locomotion speed (Fig. 1b,c, Movie 1). Both patterned and sustained activation of ChR2 were effective in promoting speed (patterned: +0.52 ± 0.31-fold, n = 11 mice, p = 0.0049; sustained: +0.79 ± 0.28-fold, n = 12 mice, p = 0.00049). The motor responses induced by the two protocols were not statistically
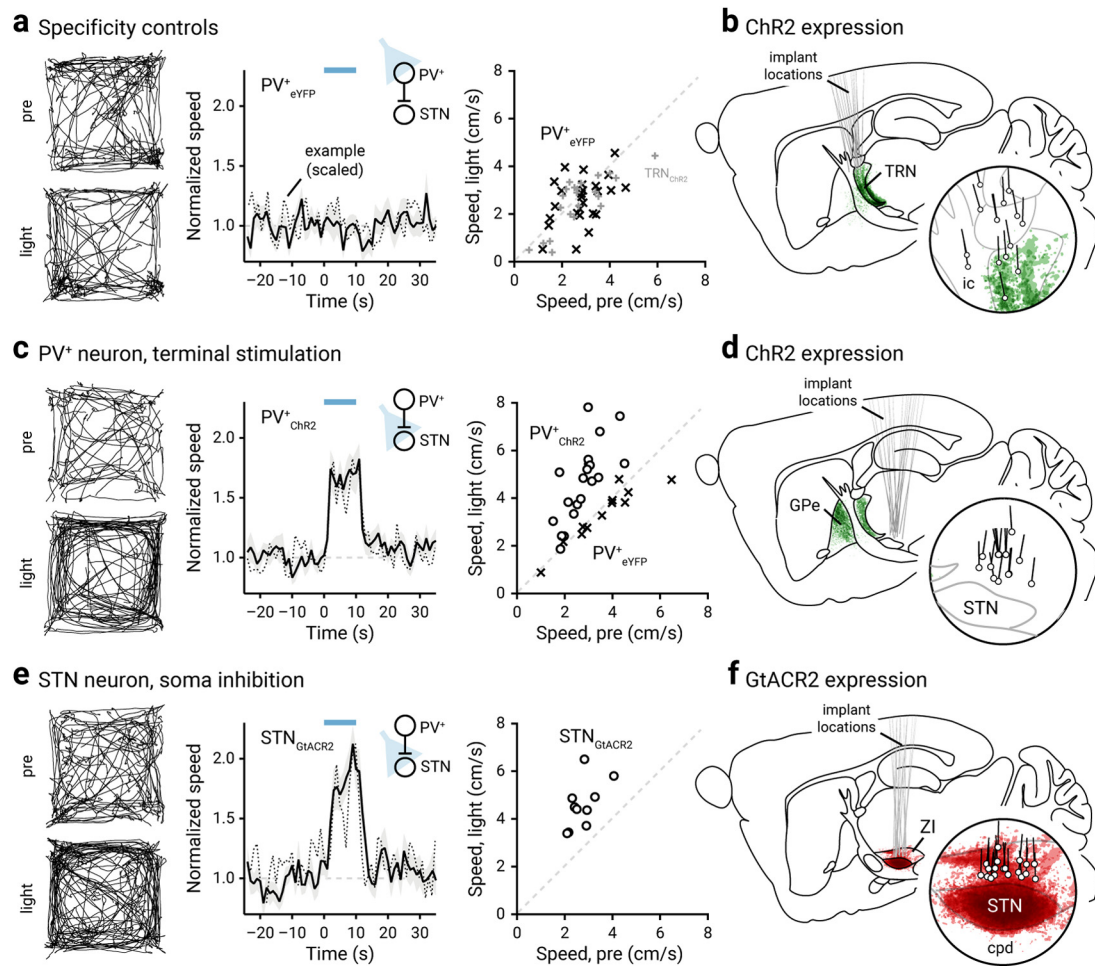
**Figure 2.** Inhibition of STN promotes locomotion. **a,** Left, Movement tracks corresponding to the pre-period (top) and light-period (bottom). Six representative mice (10 trials from each) are presented. Middle, A plot showing the relationship between normalized speed and time. Blue bar indicates the duration (10 s) of light delivery. The dotted horizontal line indicates the baseline locomotor activity level. Black solid trace is the population mean calculated from all mice; shading indicates the SEM. Black dotted trace is a representative example from a single mouse; data were scaled to facilitate comparison. The same presentation scheme is used in **c** and **e.** Data from eYFP-expressing PV-Cre mice are shown; light was delivered to the GPe. Data from the same mice (crosses) are presented on the right in a scatterplot, which shows the speed during light delivery versus speed during pre-period. Mice with ChR2-expressed in TRN neurons are used as additional controls (gray pluses). **b,** Representation of targeted ChR2-eYFP expression patterns and fiber-optic implant locations in PV-Cre mice ($n = 11$). The TRN was targeted in these experiments. **c,** Left, middle, Data from optogenetic stimulation of PV$^+$ neuron terminals in the STN are shown. Right, eYFP-expressing mice (in PV$^+$ neurons) were used as controls (crosses). **d,** Representation of ChR2-eYFP expression patterns and fiber-optic implant locations in PV-Cre mice ($n = 10$). ChR2-expressing PV$^+$ neuron terminals in the STN were targeted. **e,** Data from optogenetic inhibition of STN neurons with GtACR2 are shown. **f,** Representation of GtACR2-FusionRed expression patterns and fiber-optic implant locations in C57BL/6J mice ($n = 10$). The STN was targeted in these experiments. cpd, Cerebral peduncle; ic, internal capsule.

different ($p = 0.094$). The motor effect was readily reversed following the cessation of light delivery, as the speed during the post-period was not different from that during the pre-period. The motor response was not the result of nonspecific effects of light delivery, such as heat artifacts (Owen et al., 2019), as PV-Cre mice transduced with a control AAV (eYFP only) did not display any motor effects with light delivery (patterned: –0.035 ± 0.25-fold, $n = 13$ mice, $p = 0.84$; sustained: –0.14 ± 0.20-fold, $n = 13$ mice, $p = 0.17$; Figs. 1b, 2a, Movie 2). Similarly, sham-injected PV-Cre mice did not show any motor responses associated with light delivery (patterned: +0.11 ± 0.20-fold, $n = 11$ mice, $p = 0.28$; sustained: –0.16 ± 0.31-fold, $n = 9$ mice, $p = 0.91$).

By examining the statistics of spontaneous (pre-period) and induced locomotion (light-period), it became clear that optogenetic stimulation induced a rightward shift in the speed distribution (Fig. 1d). Furthermore, mice also showed a decrease in time spent immobile (i.e., horizontal displacement ≤ 1 cm/s) on optogenetic stimulation of PV$^+$ neurons (pre-period: 34 ± 21%; light-period: 11 ± 9.5%; $n = 230$ trials, $p < 0.0001$). Though mice

spend a larger fraction of time ambulating at higher velocities during induced locomotion, the activity level spanned the same range as observed during spontaneous locomotion. These salient features of the relationship between the activity during pre-period and light-period are not always captured at single-animal analyses. As demonstrated by the example in Figure 1b, strong motor effects were observed in trials only when low ambulatory levels occurred immediately preceding the optogenetic stimulus. To gain deeper insights into how spontaneous locomotor activity level shaped the size of the motor response, we analyzed data from individual trials. As shown in Figure 1e, the speed in the light-period was distinct from their pre-period level; most of the data points are above unity. On the contrary, eYFP controls did not display any motor effects associated with light delivery (bottom left); all data points are distributed evenly along the unity. An important feature in these data is the strong negative relationship between prestimulus speed and the fold increase in locomotion. As illustrated in Figure 1e, this relationship can be described by a monoexponential function. Furthermore, logistic

**Movie 2.** *In vivo* light delivery in PV-Cre mice transduced with a control AAV (eYFP only) did not affect locomotion. Representative movie of a mouse in an open field arena showing the lack of effect in locomotion upon light delivery to $PV^+$ neurons with no opsin expression. Behavior from two consecutive trials is shown. Video is shown at $2\times$ speed. [View online]
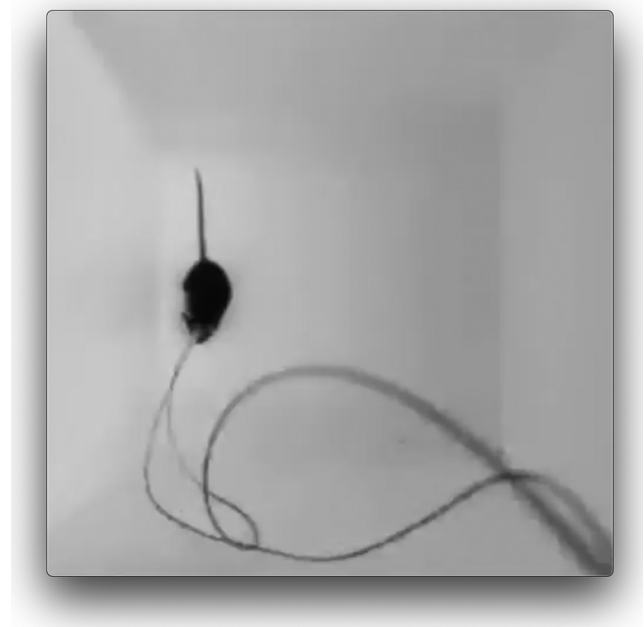


**Movie 3.** *In vivo* optogenetic inhibition of STN neurons promoted locomotion. Representative movie of a mouse in an open field arena showing increased locomotion upon optogenetic inhibition of STN neurons. Behavior from two consecutive trials is shown. Video is shown at $2\times$ speed. [View online]

**Table 4. Summary of logistic regression models**

| Strain, manipulation | Fold changes | OR | p Value | 95% confidence interval for ORs | |
|---|---|---|---|---|---|
| | | | | Lower bound | Upper bound |
| PV-Cre ChR2 | | | | | |
| | 0.1-fold increase | 0.569 | **<0.001** | 0.465 | 0.696 |
| | 1-fold increase | 0.283 | **<0.001** | 0.201 | 0.398 |
| | 10-fold increase | 3.319e−4 | **0.0093** | 0.000 | 0.138 |
| PV-Cre ChR2, 6-OHDA | | | | | |
| | 0.1-fold increase | 0.673 | **0.0012** | 0.530 | 0.856 |
| | 1-fold increase | 0.388 | **<0.001** | 0.278 | 0.541 |
| | 10-fold increase | 9.736e−7 | **0.0012** | 0.000 | 0.004 |
| Npas1-Cre-tdTom ChR2 | | | | | |
| | 0.1-fold decrease | 1.589 | **<0.001** | 1.288 | 1.960 |
| | 0.5-fold decrease | 1.589 | **<0.001** | 1.288 | 1.960 |
| | 0.8-fold decrease | 1.227 | 0.16 | 0.923 | 1.631 |

OR, Odds ratio. The bold p values are significant (i.e., <0.05).

regression predicted the motor effect when prestimulus speed was considered as a covariate (Fig. 1e, Table 4). *Post hoc* histologic examination confirmed that the behavioral effects were because of specific targeting of the GPe (Fig. 1a). As viral spread to the thalamic reticular nucleus (TRN) was apparent in some cases, we examined whether our results were confounded. Using near-identical procedures, we found that selective ChR2 expression in the TRN did not yield consistent motor effects (patterned: –0.12 ± 0.22-fold, n = 11 mice, p = 0.90; sustained: –0.17 ± 0.21-fold, n = 11 mice, p = 0.41; Fig. 2a,b).

$PV^+$ neurons send inhibitory projections primarily to the STN and SNr (Bevan et al., 1998; Sato et al., 2000a; Kita, 2007; Mastro et al., 2014; Hernández et al., 2015; Fujiyama et al., 2016; Saunders et al., 2016; Oh et al., 2017; Abecassis et al., 2020). To

confirm that the movement-promoting effects of $PV^+$ neuron stimulation were mediated through inhibiting these downstream targets, we optogenetically stimulated $PV^+$ neuron axon terminals in the STN (Fig. 2c,d). As expected, stimulation of $PV^+$ axon terminals in the STN resulted in an increase in the speed of movement (patterned: +0.41 ± 0.16-fold, n = 10 mice, p = 0.0020; sustained: +0.84 ± 0.11-fold, n = 10 mice, p = 0.0020). Light delivery at the $PV^+$ axon terminals in the STN of PV-Cre mice transduced with a control AAV (eYFP only) did not produce any motor effects with light delivery (patterned: –0.0052 ± 0.10-fold, n = 6 mice, p > 0.99; sustained: –0.081 ± 0.027-fold, n = 6 mice, p = 0.31; Fig. 2c). To exclude action potential propagation as a confound, we activated virally expressed GtACR2 (an inhibitory opsin) (Govorunova et al., 2015; Mahn et al., 2018) in STN neurons to mimic the inhibitory action of the GPe-STN input. As expected, we observed an increase in movement (+0.60 ± 0.16-fold, n = 10 mice, p = 0.0020; Fig. 2e,f, Movie 3). In sum, our data collectively argue that the activity of $PV^+$ neurons promoted locomotion via the inhibition of their primary downstream targets.

### $Npas1^+$ neurons suppress movement

In contrast with the motor effect of $PV^+$ neurons, *in vivo* optogenetic stimulation of $Npas1^+$ neurons induced a decrease in the duration of movement periods (data not shown) and locomotion speed (patterned: –0.41 ± 0.10-fold, n = 14 mice, p = 0.000031; sustained: –0.37 ± 0.089-fold, n = 16 mice, p = 0.00024; Fig. 3a–c, Movie 4). The effects of optogenetic stimulation of $Npas1^+$ neurons with both a sustained light pulse and a 20 Hz train were not different (p = 0.24) in suppressing speed as the measure of motor output. This observation is consistent with our previous findings with chemogenetic stimulation of $Npas1^+$ neurons (Glajch et al., 2016). Importantly, our observations provide a causal demonstration of the proposed role of $Npas1^+$ neurons in movement suppression (Mallet et al., 2016). The optogenetically induced motor
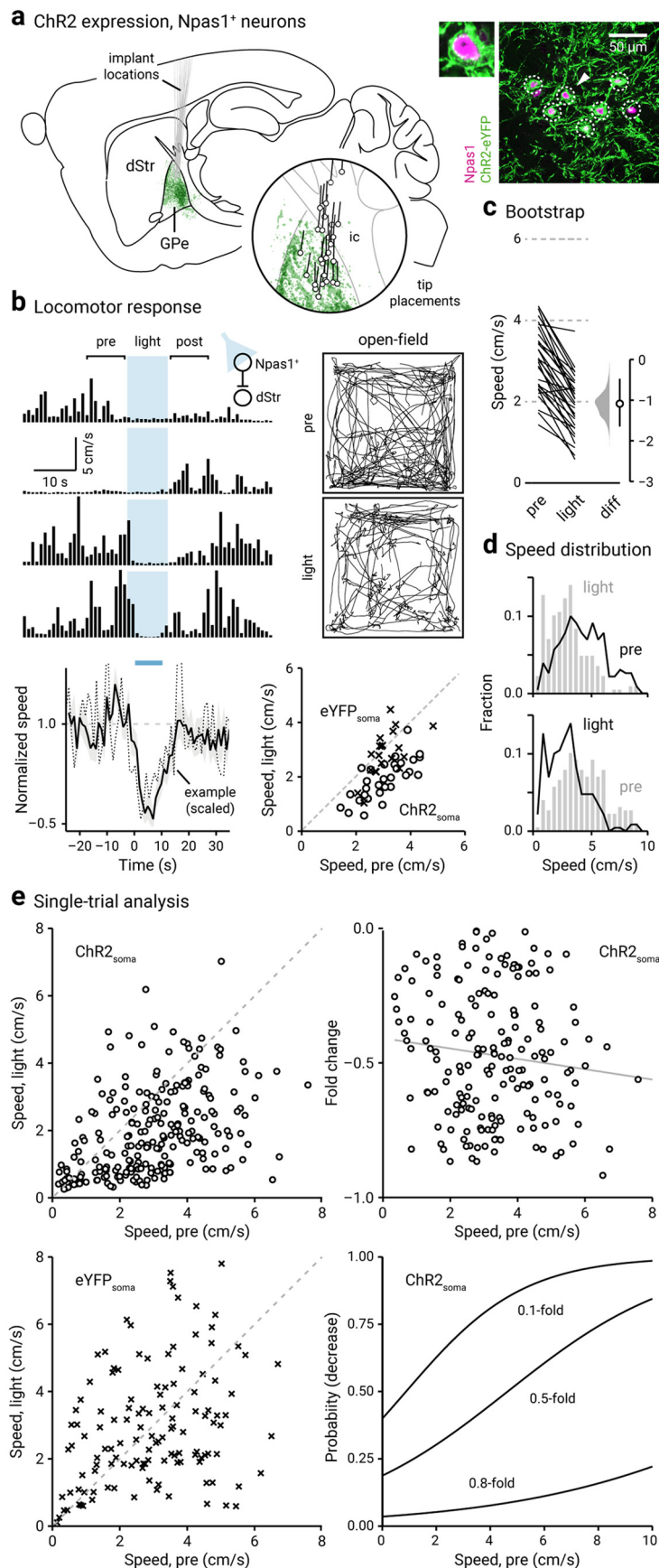
**Figure 3.** Optogenetic stimulation of Npas1^{+} neurons suppresses locomotion. *a*, Left, Representation of ChR2-eYFP expression patterns and fiber-optic implant locations in Npas1-Cre-tdTom mice (*n* = 14). Inset, Representation of optical fiber tip placements in relation to the GPe and neighboring structures. Right, Confocal micrographs showing the cellular

suppression was readily reversible, as the speed during the post-period was not different from that during the pre-period (Fig. 3*b*).

By visualizing the speed distributions during the pre-period and light-period, it is apparent that in addition to a leftward shift in the speed distribution (Fig. 3*d*), mice also showed an increase in time spent immobile on optogenetic stimulation of Npas1^{+} neurons (pre-period: 26 ± 16%; light-period: 46 ± 24%; *n* = 240 trials, *p* = 0.0020). Similar to that observed in PV^{+} neurons, single-trial data revealed that the effect size was a function of the level of spontaneous activity (i.e., during pre-period) immediately preceding the light-period. Strong motor suppression was associated with a high level of spontaneous movement preceding the light-period. This relationship can be described by a linear function (Fig. 3*e*). The magnitude of motor

←

specificity of ChR2-eYFP expression in the GPe. For clarity, a magnified example (arrowhead) is shown. ic, Internal capsule. *b*, Top, left, A representative example of the locomotor activity of a single mouse across four trials. The schematic diagram shows the site of light delivery. Blue shaded area indicates the duration (10 s) of light delivery. Top, right, Movement tracks corresponding to the pre-period (top) and light-period (bottom). Six representative mice (10 trials from each) are presented. Bottom, left, A plot showing the relationship between normalized speed and time. Blue bar indicates the duration (10 s) of light delivery. The dotted horizontal line indicates the baseline locomotor activity level. Black solid trace is the population mean calculated from all mice; shading indicates the SEM. Black dotted trace is a representative example from a single mouse; data were scaled to facilitate comparison. Bottom, right, Speed during light-period against speed during pre-period is plotted. Data from Npas1-Cre-tdTom mice expressing ChR2-eYFP (circles) and eYFP (crosses) are displayed. Each marker represents a mouse. The diagonal line indicates unity (i.e., *x* = *y*). Data points for ChR2-eYFP are systematically shifted downward relative to unity. *c*, Slopegraph showing the response of each mouse on optogenetic stimulation of Npas1^{+} neurons. The slope of each line shows the magnitude and direction of change. Median difference is plotted on a floating axis. The smoothed density represents bootstrap resampled data. The median difference is indicated as a circle, and the 95% confidence interval is indicated by the length of vertical lines. *d*, Speed distributions of mice during pre-period and light-period are shown. *e*, Top, left, A scatter plot showing the pairwise relationship between speed during light-period and speed during pre-period from Npas1-Cre-tdTom mice expressing ChR2-eYFP. Each marker is a trial. The diagonal line indicates unity. Top, right, Fold change in speed with light delivery against speed during pre-period from Npas1-Cre-tdTom mice expressing ChR2-eYFP. Each marker is a trial. Grayline is a linear fit of the data. Bottom left, A plot showing the speed during light-period versus speed during pre-period. Data from Npas1-Cre-tdTom mice expression eYFP are displayed. Each marker is a trial. The diagonal line indicates unity. Bottom, right, Probability of decrease against speed during pre-period. Logistic regression curves fitted to data for 0.1-fold, 0.5-fold, and 0.8-fold decreases are displayed.

**Movie 4.** *In vivo* optogenetic stimulation of Npas1$^+$ neurons suppressed locomotion. Representative movie of a mouse in an open field arena showing decreased locomotion upon optogenetic stimulation of Npas1$^+$ neurons. Behavior from two consecutive trials is shown. Video is shown at 2× speed. [View online]

suppression was predicted by the level of spontaneous movement with logistic regression (Fig. 3e, Table 4). On the other hand, Npas1-Cre-tdTom mice transduced with a control AAV (eYFP only) did not not statistically differ in locomotor activity with light delivery (patterned: +0.06 ± 0.19-fold, n = 11 mice, p = 0.83; sustained: –0.13 ± 0.15-fold, n = 10 mice, p = 0.13; Figs. 3b, 4a, Movie 5). Similarly, sham-injected Npas1-Cre-tdTom mice also did not show any motor responses associated with light delivery (patterned: +0.020 ± 0.081-fold, n = 6 mice, p > 0.99; sustained: +0.19 ± 0.36-fold, n = 6 mice, p > 0.99).

Next, we wanted to ask whether Npas1$^+$ neurons can bidirectionally regulate motor output. *In vivo* optogenetic inhibition of Npas1$^+$ neurons using GtACR2 induced an increase in movement (+0.34 ± 0.34-fold, n = 9 mice, p = 0.020; Fig. 4b), arguing that Npas1$^+$ neurons were exerting an ongoing inhibition of their downstream targets *in vivo*, during spontaneous locomotion. Npas1$^+$ neurons primarily project to the dStr (Kita et al., 1999; Abdi et al., 2015; Dodson et al., 2015; Hernández et al., 2015; Saunders et al., 2016; Abecassis et al., 2020). As the dStr is responsible for motor behavior (Kravitz et al., 2010; Durieux et al., 2012; Freeze et al., 2013), we stimulated Npas1$^+$ terminals within the dStr to determine whether the movement-suppressing effects of the stimulation of Npas1$^+$ neurons are mediated through this downstream projection. Similar to the effects observed with somatic stimulation of Npas1$^+$ neurons, optogenetic stimulation of their terminals in the dStr led to a reduction in movement (patterned: –0.29 ± 0.11-fold, n = 12 mice, p = 0.00049; sustained: –0.19 ± 0.14-fold, n = 12 mice, p = 0.034; Fig. 4c). In contrast, light delivery at the Npas1$^+$ neuron terminals in the dStr of Npas1-Cre-tdTom mice transduced with a control AAV (eYFP only) did not result in any motor effects (patterned: +0.058 ± 0.17-fold, n = 11 mice, p = 0.77; sustained: +0.065 ± 0.16-fold, n = 11 mice, p = 0.32).

To confirm that the motor effect induced by optogenetic manipulation of GPe output was not a result of settings unique to our experimental setup, we optogenetically stimulated dSPNs and iSPNs, respectively, in the dStr. This resulted in a canonical increase (+1.73 ± 0.21-fold, n = 8 mice, p = 0.0078) and decrease (–0.61 ± 0.077-fold, n = 8 mice, p = 0.0078) in movement, respectively, as demonstrated previously (Kravitz et al., 2010). To summarize, we conclude that ongoing Npas1$^+$ neuron activity modulates motor output—stimulation of Npas1$^+$ neurons suppressed locomotion.

## The STN preferentially targets PV$^+$ neurons

Our *in vivo* optogenetic interrogation showed that PV$^+$ neurons are movement promoting and Npas1$^+$ neurons are movement suppressing. However, the excitatory inputs that naturally drive the activity of these GPe neurons have not been fully characterized. Both anatomic and physiological studies show that the principal glutamatergic input to the GPe arises from the STN (Carpenter et al., 1981a,b; Kita and Kitai, 1987; Smith et al., 1990a,b, 1998; Kita et al., 2004; Koshimizu et al., 2013). However, it is not known whether the STN selectively targets particular GPe neuron subpopulations. Computational models suggest that the STN targets a select subset of Npas1$^+$ neurons (Bogacz et al., 2016); however, this hypothesis has yet to be empirically tested.

To study the properties of the STN–GPe input, we performed whole-cell, voltage-clamp recordings from genetically identified PV$^+$ neurons and Npas1$^+$ neurons in an acute brain slice preparation. To allow the stimulation of the STN input, an optogenetic approach was used. Injection of the STN with an AAV that expressed ChR2-eYFP constitutively led to robust ChR2-eYFP expression in STN neurons. This gave rise to eYFP-labeled axonal processes terminating throughout the GPe. The VGluT2-immunoreactive puncta on these axons suggest that they are terminating within the GPe and have the capacity to release glutamate (Fig. 5a,b). The properties of STN inputs to GPe were examined in the presence of GABAergic antagonists (10 $\mu$M SR95531, 1 $\mu$M CGP55845). Optogenetic stimulation of the STN input reliably evoked EPSCs in all neurons tested. Notably, EPSC amplitudes, as a measure of the STN input strength, were approximately five times larger in PV$^+$ neurons compared with those in Npas1$^+$ neurons (PV$^+$ = 674.01 ± 174.47 pA, n = 34 neurons; Npas1$^+$ = 128.30 ± 63.05 pA, n = 41 neurons; p < 0.0001; Fig. 5d,e). The EPSCs evoked with the constitutive ChR2 expression were not because of ectopic expression of ChR2 in the ZI, which is immediately adjacent (dorsocaudal) to the STN, as selectively targeted injection and optogenetic stimulation of the ZI input did not produce large EPSCs in either PV$^+$ neurons or Npas1$^+$ neurons (PV$^+$: 33.93 ± 27.22 pA, n = 9 neurons; Npas1$^+$: 33.08 ± 20.39 pA, n = 9 neurons; p = 0.26; Fig. 5c,d).

As the methodology used did not rely on an STN-specific driver or promoter, a Cre-lox strategy was also used to verify the specificity of the involvement of the STN in our analysis. To efficiently deliver Cre to STN neurons, we injected AAV$_{retro}$-Cre (Tervo et al., 2016) in the SNr, which is the principal downstream target of the STN (Parent and Smith, 1987; Smith et al., 1998). This Cre-delivery strategy yielded robust recombination events in STN neurons, as depicted by tdTomato expression in the Cre reporter line (LSL-tdTomato; Fig. 5f). PV-tdTom mice were then used in subsequent experiments to allow for the identification of PV$^+$ neurons (Abecassis et al., 2020). By using the same retrograde Cre-delivery strategy in conjunction with CreOn ChR2-expressing AAVs (injected into the STN), EPSCs were reliably evoked when STN input was optogenetically stimulated. Consistent with our observations using constitutive

expression of ChR2 in the STN, EPSCs evoked with the AAV$_{retro}$-Cre-mediated strategy were larger in PV$^+$ neurons than those in PV$^-$ neurons (PV$^+$: 578.92 ± 49.01 pA, $n = 6$ neurons; PV$^-$: 155.64 ± 52.61 pA, $n = 5$ neurons; $p = 0.0043$). Moreover, EPSCs measured in PV$^+$ neurons and PV$^-$ neurons in mice with Cre-mediated ChR2 expression in the STN were not different from those measured in PV$^+$ neurons and Npas1$^+$ neurons in mice with constitutive ChR2 expression in the STN (PV$^+$, Cre-induced vs PV$^+$, constitutive: $p = 0.12$; PV$^-$, Cre-induced vs Npas1$^+$, constitutive: $p = 0.51$; Fig. 5g). In summary, our experiments confirmed the validity of the general approach used in this study.

In addition to the STN, the PF Thal and PPN are known to send glutamatergic projections to the GPe (Kincaid et al., 1991; Sadikot et al., 1992; Naito and Kita, 1994; Deschênes et al., 1996; Mouroux et al., 1997; Kita et al., 2004; Yasukawa et al., 2004). We sought to compare the properties of these inputs to the STN input using near-identical approaches (see Materials and Methods). In contrast to the STN input, PF Thal and PPN inputs did not produce detectable EPSCs in all GPe neurons. Fewer PV$^+$ neurons (90.6%, 19 of 21 neurons) and Npas1$^+$ neurons (88.2%, 15 of 17 neurons) responded to PF Thal input stimulation (PV$^+$ = 76.64 ± 44.3 pA, $n = 19$ neurons; Npas1$^+$ = 45.32 ± 26.9 pA, $n = 15$ neurons) than to the STN input stimulation (Fig. 5e). Similarly, fewer PV$^+$ neurons (73.3%, 11 of 15 neurons) and Npas1$^+$ neurons (54.4%, 6 of 11 neurons) responded to PPN input stimulation (PV$^+$ = 54.75 ± 30.5 pA, $n = 11$ neurons; Npas1$^+$ = 54.32 ± 33.2 pA, $n = 6$ neurons) than to STN input stimulation (Fig. 5e). Unlike the strong neuron subtype bias in the strength of input from the STN, there was no statistical difference in the strength of inputs from PF Thal or PPN to the two GPe neuron subpopulations (PF Thal: $n_{PV}$ = 19 neurons, $n_{Npas1}$ = 15 neurons, $p = 0.54$; PPN: $n_{PV}$ = 11 neurons, $n_{Npas1}$ = 6 neurons, $p = 0.35$; Fig. 5e).

Pharmacological dissection of the synaptic responses in both PV$^+$ neurons and Npas1$^+$ neurons confirmed that the transmission at STN–GPe synapses was mediated by ionotropic glutamate receptors (Fig. 6a) as suggested by earlier studies (Kita and Kitai, 1991; Kita, 1992). Optogenetic stimulation of STN terminals in the presence of a NMDA receptor antagonist, CPP [3-((±)-2-carboxypiperazin-4-yl)propyl-1-phosphonate; 10 μM], resulted in responses with only a fast component (data not shown); CPP (10 μM) and NBQX (2,3-dihydroxy-6-nitro-7-sulfonyl-benzo[f]quinoxaline; 5 μM) completely eliminated the synaptic responses. These results were consistent with prior ultrastructural studies showing that STN terminals form AMPA
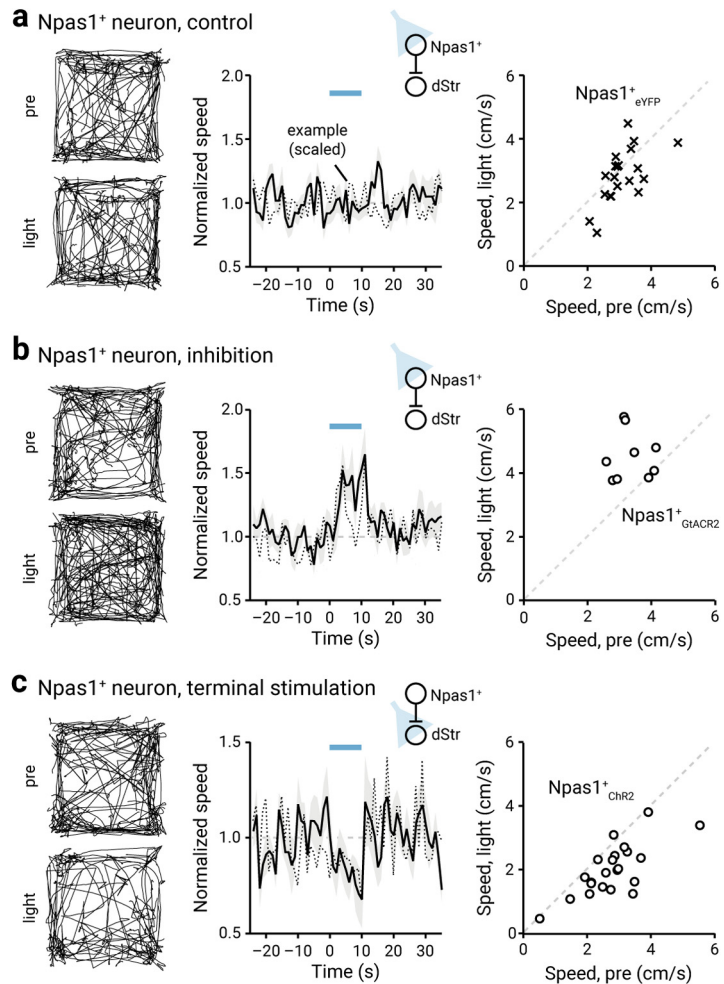


**Figure 4.** Ongoing Npas1$^+$ neuron activity suppresses locomotion. *a*, Left, Movement tracks corresponding to the pre-period (top) and light-period (bottom). Six representative mice (10 trials from each) are presented. Middle, A plot showing the relationship between normalized speed and time. Blue bar indicates the duration (10 s) of light delivery. The dotted horizontal line indicates the baseline locomotor activity level. Black solid trace is the population mean calculated from all mice; shading indicates the SEM. Black dotted trace is a representative example from a single mouse; data were scaled to facilitate comparison. The same presentation scheme is used in *b* and *c*. Data from eYFP-expressing Npas1-Cre-tdTom mice are shown; light was delivered to the GPe. *b*, Data from GtACR2-expressing Npas1-Cre-tdTom mice are shown; light was delivered to the GPe. *c*, Data from optogenetic stimulation of Npas1$^+$ neuron terminals in the dStr are shown.

and NMDA receptor-containing synapses on dendrites of GPe neurons (Bernard and Bolam, 1998; Clarke and Bolam, 1998; Koshimizu et al., 2013). Our experiments collectively showed that the STN provides the primary excitatory drive to GPe neurons, and that it is unique in its cell-targeting properties.

It is established that PV$^+$ neurons cluster in the dorsolateral regions of the GPe (Hernández et al., 2015; Saunders et al., 2016; Karube et al., 2019; Abecassis et al., 2020). In addition, anatomic tracing studies indicate that the STN input to the GPe is topographically organized (Iwamuro, 2011; Nambu, 2011). It is possible that the observed differences in the measured strength of input from STN to PV$^+$ neurons and to Npas1$^+$ neurons were because of sampling bias across different spatial subdomains within the GPe. To this end, neighboring tdTomato$^+$ and tdTomato$^-$ neurons (<150 μm apart) in both PV-L-tdTom (PV-Cre;LSL-tdTom) and Npas1-Cre-tdTom mice were sampled. EPSC amplitudes in PV$^+$ neurons were consistently larger than those in PV$^-$ neurons (PV$^+$: 674.01 ± 174.47 pA, $n = 34$ neurons; PV$^-$: 136.38 ± 60.94 pA, $n = 12$ neurons, $p < 0.0001$; Fig. 6d). On

**Movie 5.** *In vivo* light delivery in Npas1-Cre-tdTom mice transduced with a control AAV (eYFP only) did not affect locomotion. Representative movie of a mouse in an open field arena showing the lack of effect in locomotion upon light delivery to Npas1$^+$ neurons with no opsin expression. Behavior from two consecutive trials is shown. Video is shown at 2× speed. [View online]

the other hand, Npas1$^+$ neurons had smaller EPSC amplitudes than Npas1$^-$ neurons (Npas1$^+$: 128.30 ± 63.05 pA, $n = 41$ neurons; Npas1$^-$: 784.82 ± 191.25 pA, $n = 16$ neurons; $p < 0.0001$; Fig. 6d).

### STN–PV$^+$ input is weakened in a chronic model of PD

The STN–GPe network shows abnormally synchronized oscillations in both patients and animal models of PD (Hurtado et al., 1999; Plenz and Kital, 1999; Brown, 2006). Critically, both STN lesioning and deep brain stimulation abolish these pathologic oscillatory activities and have profound therapeutic benefits in alleviating the motor symptoms of PD (Bergman et al., 1990; Hurtado et al., 1999; Vitek et al., 2004, 2012; Brown, 2006; Kühn et al., 2006). Despite the clinical importance of the STN–GPe network, biophysical description of the alterations of the STN–GPe input in PD remains to be established. To this end, we examined the STN input to PV$^+$ neurons and Npas1$^+$ neurons in the chronic 6-OHDA lesion model of PD. Similar to the observations in naïve mice, the STN input to PV$^+$ neurons was stronger than that to Npas1$^+$ neurons in chronic 6-OHDA-lesioned mice, as measured by EPSC amplitude. Importantly, STN input to PV$^+$ neurons was selectively reduced in chronic 6-OHDA-lesioned mice (469.12 ± 154.33 pA, $n = 36$ neurons, $p < 0.0001$; Fig. 6a–d); this difference was observed across a range of stimulation intensities. On the contrary, STN input to Npas1$^+$ neurons did not show a detectable difference (113.28 ± 58.47 pA, $n = 37$ neurons, $p = 0.91$; Fig. 6a–d).

The neuronal makeup of the STN is generally thought to be homogeneous (Yelnik and Percheron, 1979; Hammond and Yelnik, 1983; Saunders et al., 2016). However, recent studies show that STN neurons are more heterogeneous than previously expected (Sato et al., 2000b; Koshimizu et al., 2013; Xiao et al., 2015; Papathanou et al., 2019). Although single axons can display target cell-specific properties (Shigemoto et al., 1996; Patel et al.,

2013; Sun et al., 2018), an alternative explanation for the differences in the STN input to PV$^+$ neurons and Npas1$^+$ neurons in naïve mice and their alterations in chronic 6-OHDA-lesioned mice could be because of cell-specific alterations in postsynaptic receptor properties. Therefore, we biophysically isolated AMPA and NMDA receptor-dependent currents to measure their relative contribution to the synaptic responses to STN input in PV$^+$ neurons and Npas1$^+$ neurons. In addition, we compared these AMPA and NMDA measurements to those of a well studied glutamatergic synapse—the corticostriatal synapse (Fig. 6e,f). In naïve mice, both AMPA and NMDA receptor-mediated EPSCs in PV$^+$ neurons were larger than those in Npas1$^+$ neurons (AMPA current: PV$^+$ = 685.06 ± 155.03 pA, $n = 22$ neurons; Npas1$^+$ = 141.11 ± 45.53 pA, $n = 18$ neurons; $p < 0.0001$; NMDA current: PV$^+$ = 172.30 ± 54.26 pA, $n = 22$ neurons; Npas1$^+$ = 62.19 ± 38.39 pA, $n = 18$ neurons; $p < 0.0001$; Fig. 6f,g). The AMPA-NMDA ratio of PV$^+$ neurons was also larger than that in Npas1$^+$ neurons (PV$^+$ = 3.96 ± 0.82, $n = 22$ neurons; Npas1$^+$ = 1.82 ± 0.45, $n = 18$ neurons; $p < 0.0001$). The AMPA-NMDA ratio of the STN–PV$^+$ input was larger than that observed at the corticostriatal synapse (dSPN = 3.09 ± 0.40, $n = 10$ neurons, $p = 0.014$; iSPN = 2.14 ± 0.52, $n = 16$ neurons; $p < 0.0001$; Fig. 6e,f). The difference in the AMPA-NMDA ratio in PV$^+$ neurons and Npas1$^+$ neurons indicates that different receptor complements mediate the transmission.

Both AMPA and NMDA receptor-mediated currents in PV$^+$ neurons were reduced in chronic 6-OHDA-lesioned mice compared with naïve mice (AMPA current = 430.79 ± 150.51 pA, $n = 27$ neurons, $p = 0.00030$; NMDA current = 116.94 ± 54.69 pA, $n = 27$ neurons, $p = 0.024$; Fig. 6f,g). This appeared to be a coordinated regulation, as the AMPA-NMDA ratio was not statistically different in chronic 6-OHDA-lesioned mice (PV$^+$ = 3.62 ± 0.55, $n = 27$ neurons, $p = 0.18$; Fig. 6f,g). In contrast with the findings in PV$^+$ neurons, AMPA and NMDA receptor-mediated currents were not statistically different in Npas1$^+$ neurons following chronic 6-OHDA lesioning (AMPA current = 122.07 ± 52.31 pA, $n = 17$ neurons, $p = 0.73$; NMDA current = 84.35 ± 33.69 pA, $n = 17$ neurons, $p = 0.81$; Fig. 6f,g).

Given the decrease in the functional connectivity of the STN-PV$^+$ input, we expect to see a correlated anatomic alteration following chronic 6-OHDA lesion. Contrary to our prediction, we did not find an expected decrease in the density of STN axonal fibers in the GPe following the chronic 6-OHDA lesioning (naïve, lateral = 3.61 ± 0.23 × 10$^7$ a.u., $n = 6$ mice; 6-OHDA, lateral = 3.89 ± 0.63 × 10$^7$ a.u., $n = 7$ mice; $p = 0.23$; naïve, intermediate = 3.80 ± 0.90 × 10$^7$ a.u., $n = 6$ mice; 6-OHDA, intermediate = 4.21 ± 0.26 × 10$^7$ a.u., $n = 8$ mice; $p = 0.75$; naïve, medial = 2.40 ± 0.88 × 10$^7$ a.u., $n = 6$ mice; 6-OHDA, medial = 2.66 ± 0.47 × 10$^7$ a.u., $n = 8$ mice; $p = 0.66$; Fig. 7a,b). As the density of the STN–GPe axons may not be tightly associated with the number of release sites, we then examined the abundance of putative STN–GPe boutons. By measuring density of eYFP-labeled puncta that were immunopositive for VGluT2, we found a decrease in the density of STN presynaptic boutons in the GPe following chronic 6-OHDA lesioning (naïve = 5.1 ± 0.98 counts/μm$^3$, $n = 15$ sections; 6-OHDA = 3.6 ± 1.2 counts/μm$^3$, $n = 17$ sections; $p = 0.028$; Fig. 7c). This finding corroborated the decrease in both AMPA and NMDA receptor currents in PV$^+$ neurons (Fig. 6g). Although alterations in the release probability and quantal properties of the STN–GPe synapse cannot be excluded, our data collectively show a loss of STN–GPe connectivity in a chronic model of PD.
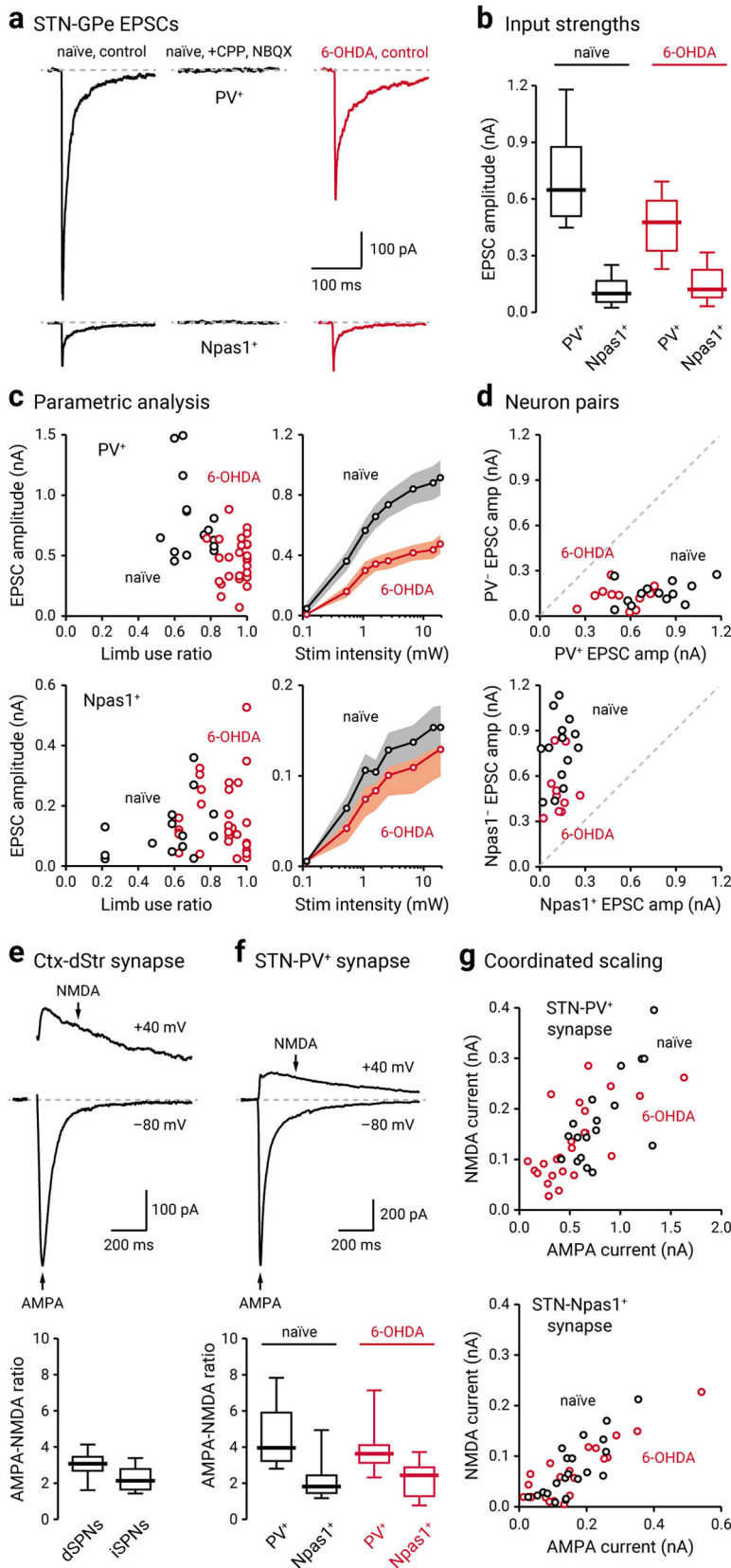
In light of the difference in the STN input to the two GPe neuron classes, we examined whether STN input also causes distinct changes in the activity of $PV^+$ neurons and $Npas1^+$ neurons. We monitored the firing of GPe neurons in response to optogenetic stimulation of the STN input. Consistent with our prior work (Hernández et al., 2015; Abecassis et al., 2020), $PV^+$ neurons and $Npas1^+$ neurons have distinct basal activity levels ($PV^+$: baseline$_{naïve}$ = 18.26 ± 3.74 Hz, $n$ = 23 neurons; $Npas1^+$: baseline$_{naïve}$ = 8.91 ± 2.97 Hz, $n$ = 10 neurons; $p < 0.0001$; Fig. 8a,b). In response to optogenetic stimulation of the STN input, both $PV^+$ neurons and $Npas1^+$ neurons showed increases in their firing ($PV^+$: stim$_{naïve}$ = 51.48 ± 6.93 Hz, $n$ = 23 neurons, $p < 0.0001$; $Npas1^+$: stim$_{naïve}$ = 31.68 ± 4.95 Hz, $n$ = 10 neurons, $p = 0.0020$; Fig. 8a,b). In naïve mice, the fold change in the firing of $PV^+$ neurons and $Npas1^+$ neurons with STN stimulation was not different ($PV^+$ naïve: +3.09 ± 0.90-fold, $n$ = 23 neurons; $Npas1^+$ naïve: +3.87 ± 1.13-fold, $n$ = 10 neurons; $p = 0.48$). In 6-OHDA lesioning, optogenetic stimulation of STN input also resulted in increases in the firing of $PV^+$ neurons and $Npas1^+$ neurons ($PV^+$: baseline$_{6-OHDA}$ = 20.79 ± 2.97 Hz, stim$_{6-OHDA}$ = 50.49 ± 9.90 Hz, $n$ = 15 neurons, $p < 0.0001$; $Npas1^+$: baseline$_{6-OHDA}$ = 5.94 ± 1.98 Hz, stim$_{6-OHDA}$ = 16.83 ± 4.95 Hz, $n$ = 11 neurons, $p = 0.0010$). Consistent with a weakening of the STN–$PV^+$ input, $PV^+$ neurons showed a selective reduction in the fold change of firing following a chronic 6-OHDA lesion ($PV^+$: stim$_{naïve}$ = +3.09 ± 0.90-fold, $n$ = 23 neurons; stim$_{6-OHDA}$ = +2.38 ± 0.27-fold, $n$ = 15 neurons; $p = 0.0049$; Fig. 8a,b). In contrast, $Npas1^+$ neurons did not show a change in the fold change in their firing between naïve and chronic 6-OHDA lesions ($Npas1^+$: stim$_{naïve}$ = +3.87 ± 1.13-fold, $n$ = 10 neurons; stim$_{6-OHDA}$ = +2.98 ± 0.96-fold, $n$ = 11 neurons; $p = 0.24$).

## Stimulation of $PV^+$ neurons lessens hypokinetic symptoms

In agreement with the established relationship between STN activity and movement suppression (Hamani et al., 2004; Aron and Poldrack, 2006; Aron et al., 2007; Eagle et al., 2008; Schmidt
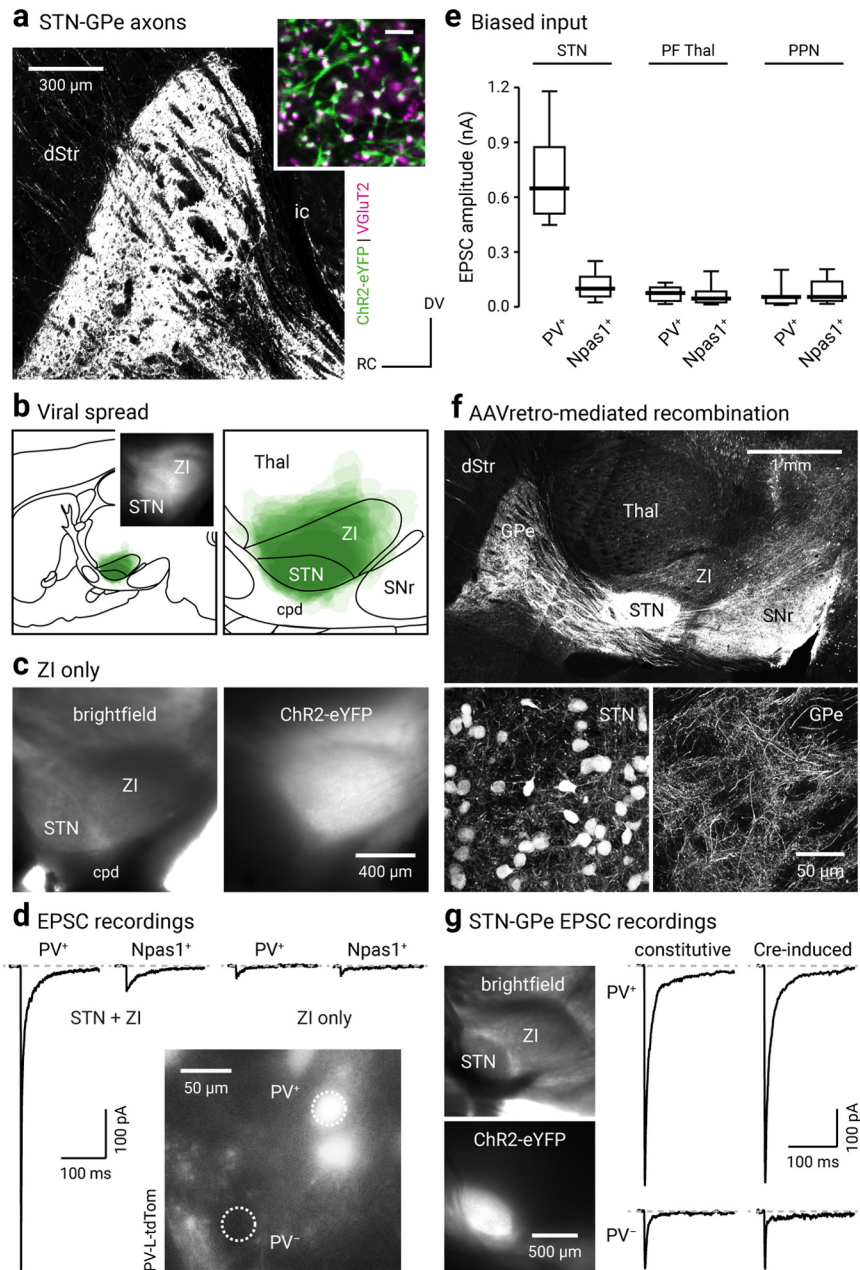


**Figure 5.** STN input is biased toward $PV^+$ neurons. ***a***, A confocal micrograph of a sagittal brain section showing eYFP-labeled STN axons in the GPe (in a mouse injected with a ChR2-eYFP AAV in the STN). Inset, High-magnification confocal micrograph showing the spatial relationship between eYFP-labeled STN axons (green) and VGluT2 (magenta) labeling. Scale bar, 5 μm. ***b***, Left, A schematic showing viral spread overlaid for each subject ($n$ = 9) used for *ex vivo* experiments. Inset, A representative epifluorescent image of a parasagittal acute brain slice showing the expression of ChR2-eYFP in the STN and the neighboring areas. Right, A magnified view of transduced areas is shown. ***c***, Left, A bright-field image of a parasagittal acute brain slice showing STN and ZI. Right, eYFP signal from the same slice showing transduction only in the ZI but not the STN. ***d***, EPSCs recorded in $PV^+$ neurons and $Npas1^+$ neurons in mice that had STN + ZI and ZI only transductions. Inset, Epifluorescence image from *ex vivo* tissue showing the GPe of a PV-L-tdTom mouse with tdTomato+ ($PV^+$) and tdTomato− ($PV^-$) neurons within the same field. ***e***, Box plots summarizing the amplitude of EPSCs recorded in $PV^+$ neurons and $Npas1^+$ neurons with optogenetic stimulation of terminals from the STN, the PF Thal, or the PPN. ***f***, Top, A montage of confocal micrographs from a sagittal brain section in a mouse injected with AAV$_{retro}$-Cre in the SNr, along with CreOn ChR2-eYFP-expressing AAVs in the STN. These images show that eYFP-labeled STN axons are arborized throughout the GPe and SNr. Bottom, High-magnification images showing eYFP-labeled neurons in the STN (left) and their axons in the GPe (right). ***g***, Left, CreOn expression of ChR2-eYFP in the STN (top), where eYFP labeling (bottom) is localized within the STN. Right, Representative EPSC recordings from voltage-clamped $PV^+$ neurons (top) and $PV^-$ neurons (bottom) in mice with constitutive (left) or CreOn (right) expression of ChR2-eYFP in the STN. cpd, Cerebral peduncle; ic, internal capsule.
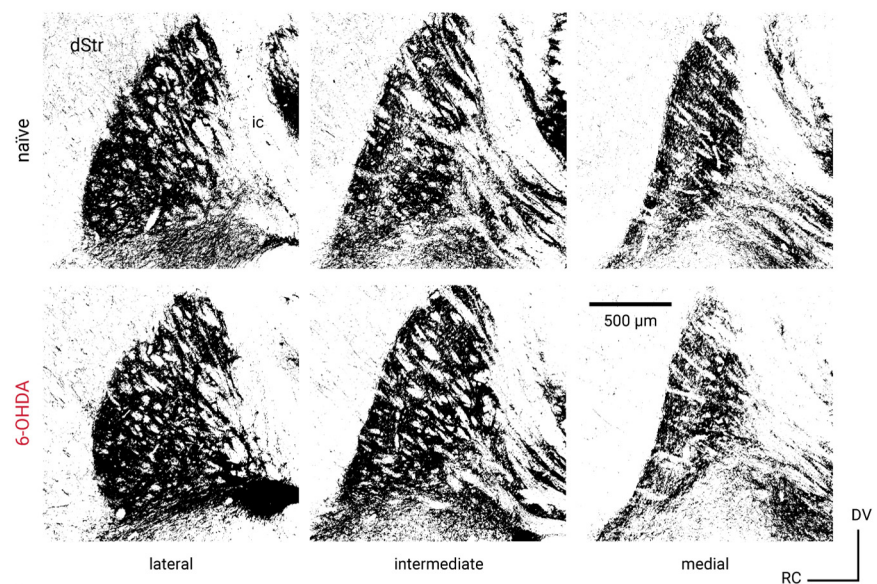
et al., 2013; Schweizer et al., 2014; Fife et al., 2017; Wessel and Aron, 2017; Adam et al., 2020), both direct recordings and theoretical models assert that the hypokinetic symptoms of PD are a result of excessive STN activity (Albin et al., 1989; Bergman et al., 1994, 1998; Wichmann and DeLong, 1996; Obeso et al., 2000; DeLong and Wichmann, 2007, 2015; Zaidel et al., 2009; Sharott et al., 2014; McGregor and Nelson, 2019). Importantly, lesioning and inactivation studies from animal models of PD further support this idea (Levy et al., 2001; Yoon et al., 2014; but see McIver et al., 2019). In other words, the weakening of the STN–PV$^+$ input that we observed in the chronic 6-OHDA-lesioned mice *ex vivo* can thus be a form of homeostatic scaling in response to the increased excitatory drive. However, this alteration may, in fact, be maladaptive as it would lead to decreased inhibitory output from the GPe to the STN. The resultant increased STN activity would in turn lead to motor suppression. If our interpretation is correct, then optogenetic stimulation of PV$^+$ neurons, which would inhibit STN neurons, should restore motor activity in chronic 6-OHDA-lesioned mice. Chronic 6-OHDA-lesioned mice have a reduced basal ambulatory activity (naïve =

←

(top) or Npas1$^+$ neurons (bottom) were plotted against limb use ratio, which provides a measure of the extent of the lesion. Each marker indicates a cell. Right, Input–output curves from EPSCs measured from PV$^+$ neurons (top) and Npas1$^+$ neurons (bottom). Each circle represents the mean EPSC amplitude measured at a particular light intensity, and the shaded area indicates SEM. *d*, Top, EPSC amplitudes measured from neighboring (within 150 μm apart) PV$^+$ neurons and PV$^-$ neurons in naïve (black) and chronic 6-OHDA-lesioned (red) PV-L-tdTom mice. Bottom, EPSC amplitudes measured from neighboring Npas1$^+$ neurons and Npas1$^-$ neurons in naïve (black) and chronic 6-OHDA-lesioned (red) Npas1-Cre-tdTom mice. Each marker represents a pair of positively and negatively identified neurons recorded from the same field. The dashed line represents the unity line. *e*, Top, Representative synaptic responses from a voltage-clamped SPN in the dStr. Corticostriatal (Ctx-Str) EPSCs were evoked with electrical stimulation; stimulus artifacts are not displayed. The gray line represents the baseline. Neurons were voltage clamped at −80 and +40 mV to measure AMPA and NMDA receptor-dependent currents, respectively. The stimulation artifact was removed for clarity. Bottom, Population data for AMPA-NMDA ratio in dSPNs and iSPNs. *f*, Top, Representative synaptic responses from a voltage-clamped PV$^+$ neuron. EPSCs were measured with optogenetic stimulation of STN input. Note the relatively small NMDA current in the STN–PV$^+$ input. Bottom, Population data for AMPA-NMDA ratio in PV$^+$ neurons and Npas1$^+$ neurons with stimulation of STN terminals in naïve (black) and chronic 6-OHDA-lesioned (red) mice. *g*, The relationship between NMDA current and AMPA current in PV$^+$ neurons (top) and Npas1$^+$ neurons (bottom; with stimulation of STN input) in naïve (black) and chronic 6-OHDA-lesioned (red) mice. Each marker represents a cell.

**Figure 6.** STN–GPe input is weakened following chronic 6-OHDA lesion. *a*, Left, Representative voltage-clamped recordings of a PV$^+$ neuron (top) and a Npas1$^+$ neuron (bottom) in naïve mice (black) showing that optogenetic stimulation of STN terminals evoked EPSCs. Middle, Application of CPP (10 μM) and NBQX (5 μM) completely eliminated the evoked EPSCs. Right, Representative EPSC recordings from a voltage-clamped PV$^+$ neuron and a Npas1$^+$ neuron in a chronic 6-OHDA lesioned mouse (red). *b*, Population data showing EPSC amplitudes measured from PV$^+$ neurons and Npas1$^+$ neurons. Data from naïve (black) and chronic 6-OHDA-lesioned (red) mice are shown. *c*, Left, EPSC amplitudes of PV$^+$ neurons
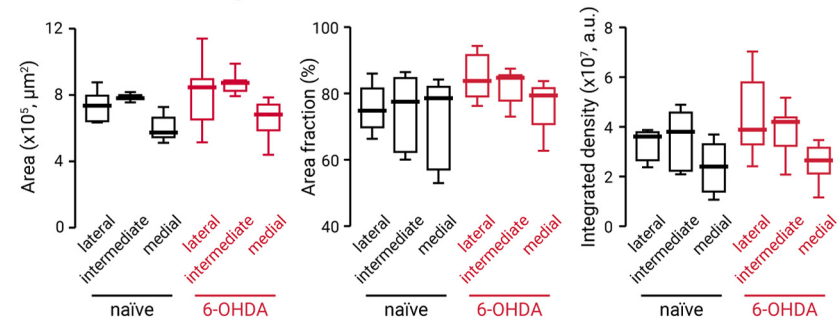
$2.62 \pm 0.86$ cm/s, $n = 12$ mice; 6-OHDA $= 1.72 \pm 0.38$ cm/s, $n = 14$ mice; $p = 0.011$), as expected. Under this condition, ChR2-mediated stimulation of PV$^+$ neurons increased locomotion in chronic 6-OHDA-lesioned mice (patterned: $+0.48 \pm 0.26$-fold, $n = 14$ mice, $p = 0.00037$; sustained: $+0.72 \pm 0.20$-fold, $n = 14$ mice, $p = 0.00012$); the extent of the increase was comparable to that observed in naïve mice (patterned: $p = 0.89$; sustained: $p = 0.82$; Fig. 8c,d). Moreover, stimulation of PV$^+$ neurons in 6-OHDA-lesioned mice induced motor responses similar to the spontaneous ambulatory activity in naïve mice (naïve$_{pre}$ $= 2.62 \pm 0.86$ cm/s, $n = 12$ mice; 6-OHDA$_{light}$ $= 2.57 \pm 0.69$ cm/s, $n = 14$ mice, $p = 0.22$). As shown in Figure 8e, although the net locomotor activity during the light-period was distinct from its pre-period level in chronic 6-OHDA-lesioned mice, there was an increased number of trials that showed a negative change (i.e., data points that are below unity in the $x$-$y$ scatter plots) in locomotion following the chronic 6-OHDA lesion (naïve: 44 of 230 trials, 19.1%; 6-OHDA: 76 of 280 trials, 27.1%; $p = 0.036$). Furthermore, the strong negative relationship between pre-period speed and the increase in locomotion that was observed in naïve mice was more pronounced in chronic 6-OHDA-lesioned mice. As described by a logistic regression function, the probability of observing an increased locomotion is reduced following the chronic 6-OHDA lesion (Fig. 8e, Table 4).

It has been shown previously that the stimulation of PV$^+$ neurons produced persistent motor promotion in an acute 6-OHDA lesion model (Mastro et al., 2017). However, it was unknown whether the lasting response can be generalized to the chronic 6-OHDA lesion model. Here, we examined whether the motor effects induced by optogenetic stimulation in PV$^+$ neurons were a function of previous stimulation history. As illustrated in Figure 9a, while motor promotion was readily observed (in both naïve and chronic 6-OHDA-lesioned mice) when PV$^+$ neurons were optogenetically stimulated, the magnitude of the effect was not associated with the order of the trials. This was determined by examining the trial number as a predictor variable in a logistic regression model. Critically, this analysis shows that repetitive optogenetic stimulation of PV$^+$ neurons did not lead to a sustained elevation of locomotor activity in the chronic 6-OHDA-lesioned mice. This inference was

confirmed by extending the time window for monitoring motor activity before and after the entire set of optogenetic stimuli in a subset of mice; the locomotion speed was not statistically different before and after the stimuli (pre$_{5min}$: $0.96 \pm 0.29$ cm/s, post$_{5min}$: $1.07 \pm 0.15$ cm/s, $n = 4$, $p = 0.89$; Fig. 9b). Last, a summary of motor effects under different conditions is tabulated in Table 5.
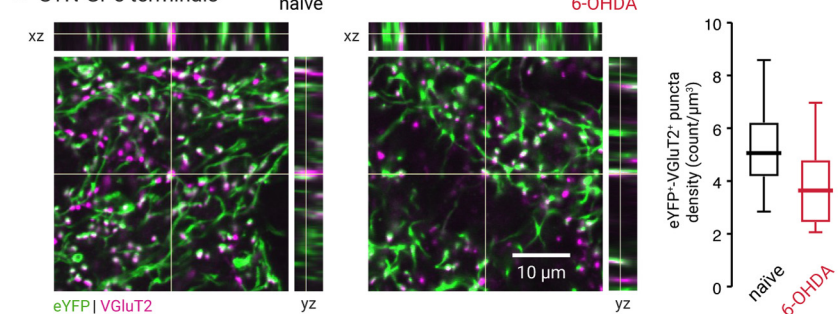


**Figure 7.** The cell type specificity of STN–GPe EPSCs is not because of topographical biasing. *a*, Confocal micrographs showing the GPe in sagittal brain sections of a naïve (top, black) or chronic 6-OHDA-lesioned (bottom, red) C57BL/6J mice with ChR2-eYFP-expressing AAVs in the STN. Lateral, intermediate, and medial sections of the GPe are shown. ic, Internal capsule. *b*, Analysis of the eYFP signal in naïve (black) and chronic 6-OHDA-lesioned (red) mice. The surface area of the GPe (left), the percentage area covered by the eYFP signal (middle), and the integrated density of the eYFP signal (right) are quantified. *c*, Left and middle, Confocal micrographs showing the density of eYFP- and VGluT2-immunoreactive elements in the GPe from naïve and chronic 6-OHDA-lesioned mice. Breakout panels show orthogonal *x*–*z* projection (top) and *y*–*z* projection (right). Crosshairs indicate the pixel of interest. The colocalization of the signals is shown as white. Right, Box plots summarize the density of putative STN–GPe terminals in naïve (black) and chronic 6-OHDA-lesioned (red) mice.

**Figure 8.** PV[+] neuron stimulation lessens hypokinetic symptoms. *a*, Top, Representative cell-attached recordings from PV^{+} neurons in naïve (left, black) and chronic 6-OHDA-lesioned (right, red) mice. Raster plots show trials from a single PV[+] neuron, where each raster corresponds to an action potential. Bottom, Representative cell-attached recordings from Npas1^{+} neurons in naïve (left, black) and 6-OHDA-lesioned (right, red) mice. Each blue square represents a 2 ms light pulse delivered to the GPe. *b*, Left, Box plots summarizing the population data from naïve

## Discussion

In this study, by optogenetically manipulating the activity of specific GPe neuron subpopulations and their downstream targets, we concluded that $PV^+$ neurons are movement promoting and $Npas1^+$ neurons are movement inhibiting. Consistent with their distinct functional roles, *ex vivo* electrophysiology further delineated that the STN input biased toward $PV^+$ neurons. By using a chronic model of PD, we showed that $PV^+$ neurons play an important role in the hypokinetic symptoms of the disease. Accordingly, optogenetic stimulation of $PV^+$ neurons restored mobility.

### GPe neuron subtypes have opposing roles in motor control

Historically, it has been challenging to assign specific functional roles to the GPe. Lesioning or inactivation studies were largely inconclusive, as these manipulations did not result in a consistent motor phenotype (Norton, 1976; Ossowska et al., 1983; Schneider and Olazabal, 1984; Hauber et al., 1998; Joel et al., 1998; Konitsiotis et al., 1998; Soares et al., 2004; Hegeman et al., 2016). A large number of studies showed that GPe neurons change their activity in relation to movement; however, the identity of the recorded neurons was unknown (DeLong, 1971; Anderson, 1978; Anderson and Horak, 1985; DeLong et al., 1985; Mitchell et al., 1987; Filion et al., 1988; Nambu et al., 1990; Mink and Thach, 1987, 1991a,b; Mushiake and Strick, 1995; Parent and Hazrati, 1995; Kimura et al., 1996; Arkadir et al., 2004; Shin and Sommer, 2010; Schmidt et al., 2013; Yoshida and Tanaka, 2016; Gu et al., 2020; Mullie et al., 2020). It has been shown that identified GPe neuron subtypes can display diverse changes in their activity during spontaneous body movements (Dodson et al., 2015). Collectively, these observational studies

---

←

(left, black) and chronic 6-OHDA-lesioned (right, red) mice. Right, Scatter plots showing the relationship between EPSC amplitude and spontaneous firing rate of $PV^+$ neurons (top) and $Npas1^+$ neurons (bottom). Data from both naïve (black) and chronic 6-OHDA-lesioned (red) mice are displayed. Each marker indicates a cell. *c*, Open field activity in response to optogenetic stimulation of $PV^+$ neurons in the GPe in chronic 6-OHDA-lesioned mice. Left, A representative example of locomotion activity of a chronic 6-OHDA-lesioned mouse across four individual trials. The schematic diagram shows the cell type and site of light delivery. Pre-period indicates 10 s before light delivery; post-period indicates 10 s after light delivery. Blue shaded area indicates the duration (10 s) of light delivery. Right, Movement tracks corresponding to the pre-period (top) and light-period (bottom). Six representative mice (10 trials from each) are presented. *d*, Left, Slopegraph showing the response of each mouse on optogenetic stimulation of $PV^+$ neurons in chronic 6-OHDA-lesioned mice. The slope of each line shows the magnitude and direction of change. Median difference is plotted on a floating axis. The smoothed density represents bootstrap resampled data. The median difference is indicated as a circle, and the 95% confidence interval is indicated by the length of vertical lines. Top, right, A plot showing the relationship between normalized speed and time. Blue bar indicates the duration (10 s) of light delivery. The dotted horizontal line indicates the normalized baseline motor activity level. Black solid trace is the average distance from all mice; the shaded area shows the SEM. Black dotted trace is a representative example from a single mouse; data were scaled to facilitate comparison. Bottom, right, Speed during light-period against speed during pre-period. Data from chronic 6-OHDA-lesioned PV-Cre mice expressing ChR2-eYFP are displayed. Each marker represents a mouse. The diagonal line indicates unity (i.e., $x = y$). 6-OHDA data points are systematically shifted upward relative to unity. Locomotor activity was higher with light delivery. Naïve data (black) from Figure 1*b* are replotted for comparison. *e*, Left, Scatter plots showing the pairwise relationship between speed during light-period and speed during pre-period in naïve (top) and chronic 6-OHDA-lesioned PV-Cre mice are shown (bottom). To facilitate comparison, data from naïve mice are replotted (top). The diagonal line indicates unity. Middle, Fold change in speed with light delivery against speed during pre-period from PV-Cre mice expressing ChR2-eYFP. Each marker represents a trial. Inset, Same data displayed with fold increase on y-axis on a log scale. Right, Logistic regression curves fitted to data for 0.1-fold, 1-fold, and 10-fold increases are displayed.

---

**a** Hysteresis
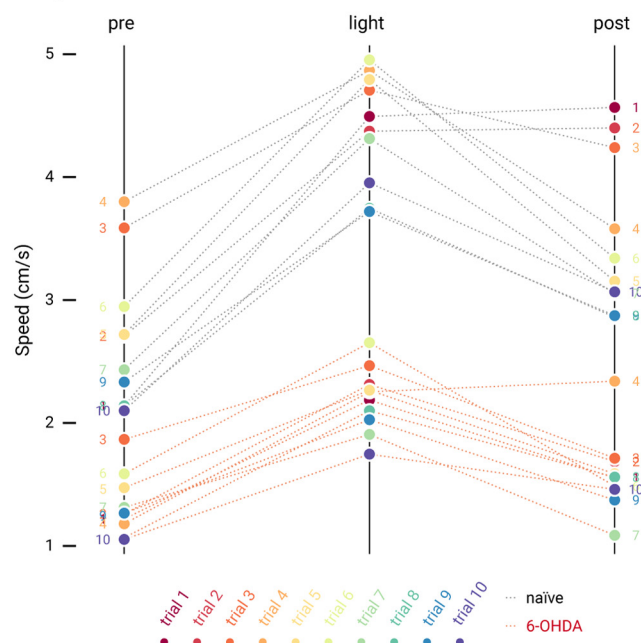
**b** Extended monitoring
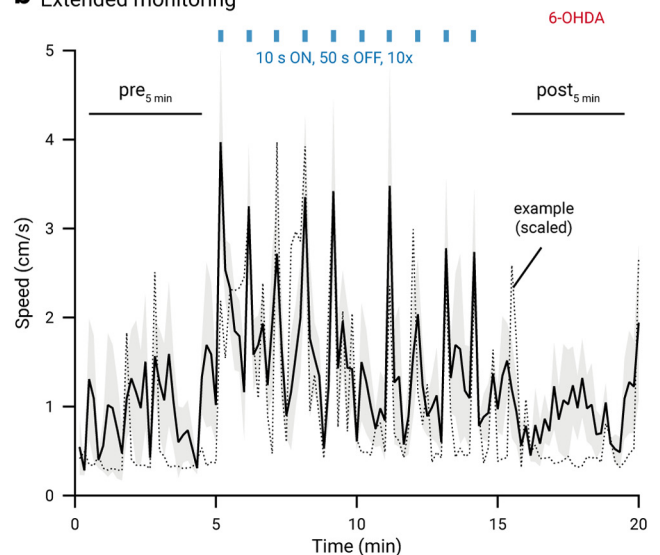
**Figure 9.** No persistent motor effects are induced by *in vivo* optogenetic stimulation in chronic 6-OHDA-lesioned mice. *a*, Slopegraph showing the size and reversibility of motor responses induced by optogenetic stimulation of $PV^+$ neurons in naïve (gray dotted lines) and chronic 6-OHDA-lesioned mice (red dotted lines). Ten trials (circles) were run on each mouse. Trial numbers are denoted by colors (rainbow). Data from sustained (naïve: $n = 12$; 6-OHDA: $n = 14$) and patterned (naïve: $n = 12$; 6-OHDA: $n = 14$) stimulation are combined. The slope of each line shows the magnitude and direction of change. *b*, A plot showing the motor activity of a subset of chronic 6-OHDA-lesioned mice ($n = 4$) across time. Blue bar indicates the duration of light delivery; 10 stimuli were delivered. Black solid trace is the average distance from all mice; the shaded area shows the SEM. Black dotted trace is a representative example from a single mouse; data were scaled to facilitate comparison.

strongly argue that GPe neurons are involved in motor control. Our data, along with our previous study, unambiguously demonstrate the causality between the activity of GPe neurons and locomotion (Glajch et al., 2016)—and importantly the opposing roles

**Table 5. Statistical summary for behavioral analyses**

| Strain, manipulation | Transgene | Injection site | Light delivery | Stim paradigm | Speed, pre (cm/s) Median ± MAD | Speed, light (cm/s) Median ± MAD | Fold change Median ± MAD | Sample size (*n*, mice) | Statistical analysis[d] *p* Value[e] (Wilcoxon test) | *p* Value[f] (Mann–Whitney *U* test) |
|---|---|---|---|---|---|---|---|---|---|---|
| PV-Cre[a,b] | ChR2-eYFP | GPe | GPe | Patterned[c] | 2.48 ± 0.64 | 3.54 ± 0.56 | +0.52 ± 0.31 | 11 | **0.0049** | |
| PV-Cre[a,b] | ChR2-eYFP | GPe | GPe | Sustained[c] | 2.52 ± 0.68 | 4.47 ± 0.72 | +0.79 ± 0.28 | 12 | **0.00049** | |
| PV-Cre | eYFP | GPe | GPe | Patterned | 2.88 ± 0.55 | 3.00 ± 0.86 | −0.04 ± 0.25 | 13 | 0.84 | **0.022**[g] |
| PV-Cre | eYFP | GPe | GPe | Sustained | 2.82 ± 0.60 | 2.48 ± 0.50 | −0.14 ± 0.20 | 13 | 0.17 | **<0.0001**[g] |
| PV-Cre | sham | GPe | GPe | Patterned | 2.06 ± 0.25 | 2.25 ± 0.38 | +0.11 ± 0.20 | 11 | 0.28 | **0.013**[g] |
| PV-Cre | sham | GPe | GPe | Sustained | 2.16 ± 0.82 | 2.25 ± 0.79 | −0.16 ± 0.31 | 9 | 0.91 | **0.0075**[g] |
| PV-Cre, 6-OHDA[b] | ChR2-eYFP | GPe | GPe | Patterned | 1.24 ± 0.39 | 1.84 ± 0.64 | +0.48 ± 0.26 | 14 | **0.00037** | 0.89[g] |
| PV-Cre, 6-OHDA[b] | ChR2-eYFP | GPe | GPe | Sustained | 1.40 ± 0.50 | 2.57 ± 0.69 | +0.72 ± 0.20 | 14 | **0.00012** | 0.82[g] |
| Npas1-Cre-tdTom[a] | ChR2-eYFP | GPe | GPe | Patterned[c] | 2.98 ± 0.66 | 1.74 ± 0.56 | −0.41 ± 0.10 | 14 | **<0.0001** | |
| Npas1-Cre-tdTom[a] | ChR2-eYFP | GPe | GPe | Sustained[c] | 3.04 ± 0.56 | 2.08 ± 0.41 | −0.37 ± 0.09 | 16 | **0.00024** | |
| Npas1-Cre-tdTom | eYFP | GPe | GPe | Patterned | 2.95 ± 0.41 | 3.08 ± 0.40 | +0.06 ± 0.19 | 11 | 0.83 | **0.00018**[h] |
| Npas1-Cre-tdTom | eYFP | GPe | GPe | Sustained | 2.89 ± 0.36 | 2.74 ± 0.56 | −0.13 ± 0.15 | 10 | 0.13 | **0.0089**[h] |
| Npas1-Cre-tdTom | sham | GPe | GPe | Patterned | 2.43 ± 0.58 | 2.52 ± 0.42 | +0.02 ± 0.08 | 6 | >0.99 | **0.0008**[h] |
| Npas1-Cre-tdTom | sham | GPe | GPe | Sustained | 3.16 ± 0.23 | 2.76 ± 0.51 | +0.19 ± 0.36 | 6 | >0.99 | **0.044**[h] |
| PV-Cre | ChR2-eYFP | GPe | STN | Patterned | 2.81 ± 0.52 | 4.34 ± 1.02 | +0.41 ± 0.16 | 10 | **0.0020** | |
| PV-Cre | ChR2-eYFP | GPe | STN | Sustained | 2.88 ± 0.47 | 5.26 ± 1.48 | +0.84 ± 0.11 | 10 | **0.0020** | |
| PV-Cre | eYFP | GPe | STN | Patterned | 3.38 ± 1.09 | 3.36 ± 1.04 | −0.00 ± 0.10 | 6 | >0.99 | **0.00025**[i] |
| PV-Cre | eYFP | GPe | STN | Sustained | 3.77 ± 0.79 | 3.54 ± 0.53 | −0.08 ± 0.03 | 6 | 0.31 | **0.00025**[i] |
| Npas1-Cre-tdTom | ChR2-eYFP | GPe | dStr | Patterned | 2.89 ± 0.45 | 1.85 ± 0.53 | −0.29 ± 0.11 | 12 | **0.00049** | |
| Npas1-Cre-tdTom | ChR2-eYFP | GPe | dStr | Sustained | 2.66 ± 0.78 | 2.17 ± 0.62 | −0.19 ± 0.14 | 12 | **0.034** | |
| Npas1-Cre-tdTom | eYFP | GPe | dStr | Patterned | 2.96 ± 0.85 | 2.98 ± 1.04 | +0.06 ± 0.17 | 11 | 0.77 | **0.0006**[j] |
| Npas1-Cre-tdTom | eYFP | GPe | dStr | Sustained | 2.68 ± 0.62 | 2.86 ± 0.97 | +0.07 ± 0.16 | 11 | 0.32 | **0.011**[j] |
| Npas1-Cre-tdTom | GtACR2 | GPe | GPe | Sustained | 3.19 ± 0.39 | 4.37 ± 0.50 | +0.34 ± 0.34 | 9 | **0.020** | |
| C57BL/6J | GtACR2 | STN | STN | Sustained | 2.67 ± 0.31 | 4.45 ± 0.60 | +0.60 ± 0.16 | 10 | **0.0020** | |

[a] Pretrial, basal ambulatory activity: PV-Cre: 2.88 ± 0.61 cm/s, *n* = 67 mice; Npas1-Cre-tdTom: 2.77 ± 0.54 cm/s, *n* = 56 mice; *p* = 0.91 (Mann–Whitney *U* test). Spontaneous locomotor activity (speed, pre-period): PV-Cre: 2.77 ± 0.61 cm/s, *n* = 67 mice; Npas1-Cre-tdTom: 2.82 ± 0.44 cm/s, *n* = 56 mice; *p* = 0.14 (Mann–Whitney *U* test). Data from all PV-Cre and Npas1-Cre-tdTom mice used in this study were pooled.
[b] Pretrial, basal ambulatory activity: PV-Cre, naïve: 2.62 ± 0.86 cm/s, *n* = 12 mice; PV-Cre, 6-OHDA: 1.72 ± 0.38 cm/s, *n* = 14 mice; *p* = 0.0037 (Mann–Whitney *U* test). Spontaneous locomotor activity (speed, pre-period): PV-Cre, naïve: 2.51 ± 0.62 cm/s, *n* = 12 mice; PV-Cre, 6-OHDA: 1.25 ± 0.35 cm/s, *n* = 14 mice; *p* = 0.000056 (Mann–Whitney *U* test).
[c] Data from patterned and sustained stimulation paradigms were compared for PV-Cre (*p* = 0.094) and Npas1-Cre-tdTom (*p* = 0.24; Mann–Whitney *U* test).
[d] Two-tailed *p* values are listed. The bold *p* values are significant (i.e., < 0.05). No multiple testing corrections were considered.
[e] Locomotor speed during pre-period and light-period from the same mice were compared.
[f] Fold changes from different experimental groups were tested. Only data obtained with the same stimulation paradigm were compared.
[g] Data were compared with PV-Cre, ChR2-eYFP, light delivery at the GPe.
[h] Data were compared with Npas1-Cre-tdTom, ChR2-eYFP, light delivery at the GPe.
[i] Data were compared with PV-Cre, ChR2-eYFP, light delivery at the STN.
[j] Data were compared with Npas1-Cre-tdTom, ChR2-eYFP, light delivery at the dStr.

played by PV$^+$ neurons and Npas1$^+$ neurons. Though we have quantified immobility in this study, we do not have quantitative information about whether optogenetic manipulations may result in altered innate behaviors (e.g., rearing, grooming, and freezing) that may confound our measurements of locomotion.

Our current data showed that in naïve mice, stimulation of PV$^+$ neurons and their terminals in the STN promoted movement. To our knowledge, this has not been previously reported. Consistent with the fact that STN neuron activity is associated with movement inhibition (Hamani et al., 2004; Aron and Poldrack, 2006; Aron et al., 2007; Eagle et al., 2008; Schmidt et al., 2013; Schweizer et al., 2014; Fife et al., 2017; Wessel and Aron, 2017; Adam et al., 2020), we showed that phasic inhibition (either synaptically or opsin mediated) of STN neurons is movement promoting. In addition, as the majority of PV$^+$ neurons send bifurcating axons to both the STN and SNr (Kita and Kitai 1994; Bevan et al., 1998; Sato et al., 2000a; Kita, 2007; Fujiyama et al., 2016; Oh et al., 2017); from a circuit organization standpoint, the PV$^+$-SNr projection is expected to reinforce the motor effects imposed by the PV$^+$-STN projection. Although our

observation is in line with the findings from our laboratory and others (Glajch et al., 2016; Mallet et al., 2016), we do not fully understand the motor suppression produced by Npas1$^+$ neurons. While Npas1$^+$ neurons have extensive axonal arborization in the dStr, their downstream impact on the excitability of striatal projection neurons is relatively weak (Glajch et al., 2016). It is possible that additional signaling partners are involved.

In this study, we drove the activity of PV$^+$ neurons or Npas1$^+$ neurons by activating ChR2. These experiments were critical to establishing the causal role of PV$^+$ neurons and Npas1$^+$ neurons in motor control. By directing light stimulus to different brain structures, we dissected circuit elements that are involved in these motor effects. While these gain-of-function experiments caused observable motor effects, they are insufficient to conclude whether the motor effects are the native functions mediated by PV$^+$ neurons and Npas1$^+$ neurons. We addressed this by performing loss-of-function experiments using GtACR2 to inhibit GPe neuron subtypes or their postsynaptic targets. GPe neurons are known to form intranuclear collaterals (Kita, 1994; Nambu and Llinás, 1997; Mallet et al., 2012;

Saunders et al., 2015). As we do not yet have the tools for the selective manipulation of these local collaterals, we will need to rely on *ex vivo* studies to assess their relevance based on the connectivity principle of these local connections. By examining moment-to-moment fluctuations in movement speed, we showed that optogenetically induced motor responses did not differ from the normal range of spontaneous locomotion displayed by mice. In sum, our *in vivo* studies reinforce the notion from prior *in vivo* electrophysiological studies that GPe neurons are critical for movement.

There are several possible biological benefits to a dual system of $PV^+$ neurons and $Npas1^+$ neurons in the GPe. It is conceivable that the two neuron populations with opposing functions form a rheostat in controlling net motor output. However, their functional relationship may not be simply antagonistic. As both initiation and termination of motor programs are equally important and are core functions of the basal ganglia (Redgrave et al., 2010; Jahanshahi et al., 2015), it is possible that $PV^+$ neurons and $Npas1^+$ neurons are differentially involved in selecting voluntary versus suppressing competing motor programs. Alternatively, GPe neuron subtypes can be selectively engaged in the regulation of antagonistic muscle groups that are necessary for the execution of one specific movement. It is reasonable to think that $PV^+$ neurons and $Npas1^+$ neurons are both involved in the selection of competing behaviors and the combination of movements that occur either jointly or in succession. Related ideas have been proposed for striatal neurons (Mink, 1996; Klaus et al., 2017, 2019; Arber and Costa, 2018). To gain further insights into this topic, it will be important in the future to determine the temporal organization of the activity of GPe neuron subtypes in relation to movement.

### The STN forms a reciprocal loop with $PV^+$ neurons

In this study, we found that the STN provides a stronger input to $PV^+$ neurons than to $Npas1^+$ neurons. This finding is supported by a recent *in vivo* electrophysiological study showing that STN strongly targets "prototypic" neurons that are predominantly $PV^+$ neurons (Ketzef and Silberberg, 2020). This is in contrast with our previous rabies-tracing study that showed a uniform STN input across GPe neuron subtypes (Hunt et al., 2018). In addition, our finding contradicts computational studies that predicted a stronger connection from the STN to a subset of $Npas1^+$ neurons (Bogacz et al., 2016; Suryanarayana et al., 2019). Given the known caveats associated with rabies-based tracing (Svoboda, 2019), this discrepancy perhaps is not completely surprising. As we found a notable input from the STN to $Npas1^+$ neurons, it is possible that the STN input regulates movement via sending an efference copy to the $Npas1^+$ neurons in addition to the primary projection to its downstream target (i.e., $PV^+$ neurons). Moreover, the difference in the AMPA-NMDA ratio of the synaptic responses in $PV^+$ neurons and $Npas1^+$ neurons indicates that the STN input to these neurons is mediated by different complements in the postsynaptic glutamate receptors.

Recent studies indicate the presence of heterogeneity in STN neurons (Sato et al., 2000b; Isoda and Hikosaka, 2008; Koshimizu et al., 2013; Xiao et al., 2015; Papathanou et al., 2019). It is possible that unique STN neurons provide inputs to distinct GPe neuron subpopulations. As we are only beginning to grasp the cellular heterogeneity within both the GPe and STN, additional work is needed to further our understanding of the organization of the STN–GPe network. As $PV^+$ neurons form the principal inhibitory innervation to the STN (Mastro et al., 2014; Abdi et al., 2015; Hernández et al., 2015; Saunders et al., 2016),

these data collectively demonstrate a closed reciprocal feedback loop formed between the STN and $PV^+$ neurons. Although earlier studies have examined the electrophysiological and anatomic properties of the STN–GPe network (Kita and Kitai, 1987, 1991; Nambu et al., 2000; Kita et al., 2004; Kita, 2007; Mastro et al., 2014; Abdi et al., 2015; Hernández et al., 2015; Saunders et al., 2016; Kovaleski et al., 2020), the cell type specificity of the STN input in the GPe was not known. Importantly, our new data add critical insights into the cellular constituents that are involved in this reciprocal loop.

In this study, we found that the STN input to $PV^+$ neurons is reduced in chronic 6-OHDA-lesioned mice. These findings are consistent with the downregulation of glutamate receptors in the GPe of PD models (Porter et al., 1994; Betarbet et al., 2000; Kaneda et al., 2005). We have previously found a decrease in the ambient glutamate content in the GPe following a chronic loss of dopamine (Cui et al., 2016); our current study adds to the literature that glutamatergic signaling in the GPe is altered in PD.

STN–GPe network function and its dysfunction in the context of PD have been widely studied. Experimental and computational studies suggest that the STN–GPe network is important for the generation and amplification of oscillatory activity (Bevan et al., 2002; Gillies et al., 2002; Terman et al., 2002; Walters et al., 2007; Mallet et al., 2008; Holgado et al., 2010; Cruz et al., 2011; Tachibana et al., 2011). Abnormally synchronized $\beta$-oscillations (i.e., 15–30 Hz) in the STN–GPe network are thought to be partially responsible for the hypokinetic symptoms of PD. Abolishing the pathologic oscillatory activity by lesioning or deep-brain stimulation of the STN or the GPe has profound therapeutic benefits in alleviating motor symptoms of PD (Albin et al., 1989; Bergman et al., 1990; Hurtado et al., 1999; Vitek et al., 2004, 2012; Kühn et al., 2006; Hammond et al., 2007; Johnson et al., 2012; McGregor and Nelson, 2019). We previously observed strengthening of the GABAergic GPe input to the STN with chronic 6-OHDA lesion (Fan et al., 2012); it is now clear that this input arises from $PV^+$ neurons as $PV^+$ neurons are the primary source of inhibitory input to the STN (Mastro et al., 2014; Hernández et al., 2015; Abecassis et al., 2020). As the activity of the STN negatively regulates motor output (Hamani et al., 2004; Aron and Poldrack, 2006; Aron et al., 2007; Eagle et al., 2008; Schmidt et al., 2013; Schweizer et al., 2014; Fife et al., 2017; Wessel and Aron, 2017; Adam et al., 2020), a decrease in the ambient glutamate content in the GPe (Cui et al., 2016), along with a reduction in the STN–$PV^+$ input, would disinhibit the STN and suppress motor output in the parkinsonian state, thus contributing to the hypokinetic symptoms of PD. On the other hand, a strengthening of the inhibitory $PV^+$ input to the STN (Chu et al., 2015) would promote movement and may act as a compensatory mechanism against the hypokinetic effects of the abnormal glutamatergic signaling in the GPe in PD. How these synaptic adaptations interact will vary depending on ongoing activity of the network and the interplay of synaptic features unique to each synapse. As we attempt to make predictions based on rate-based models, we should begin to incorporate oscillation theories with our thinking to gain critical insights into basal ganglia function and dysfunction (Wichmann et al., 2011; Wilson, 2013; Little and Brown, 2014).

## References
Abdi A, Mallet N, Mohamed FY, Sharott A, Dodson PD, Nakamura KC, Suri S, Avery SV, Larvin JT, Garas FN, Garas SN, Vinciati F, Morin S, Bezard E, Baufreton J, Magill PJ (2015) Prototypic and arkypallidal neurons in the dopamine-intact external globus pallidus. J Neurosci 35:6667–6688.

Abecassis ZA, Berceau BL, Win PH, García D, Xenias HS, Cui Q, Pamukcu A, Cherian S, Hernández VM, Chon U, Lim BK, Kim Y, Justice NJ, Awatramani R, Hooks BM, Gerfen CR, Boca SM, Chan CS (2020) Npas1 (+)-Nkx2.1(+) neurons are an integral part of the cortico-pallido-cortical loop. J Neurosci 40:743–768.

Adam EM, Johns T, Sur M (2020) Cortico-subthalamic projections send brief stop signals to halt visually-guided locomotion. bioRxiv. doi: https://doi.org/10.1101/2020.02.05.936443.

Albin RL, Young AB, Penney JB (1989) The functional anatomy of basal ganglia disorders. Trends Neurosci 12:366–375.

Albin RL, Young AB, Penney JB (1995) The functional anatomy of disorders of the basal ganglia. Trends Neurosci 18:63–64.

Anderson ME (1978) Discharge patterns of basal ganglia neurons during active maintenance of postural stability and adjustment to chair tilt. Brain Res 143:325–338.

Anderson ME, Horak FB (1985) Influence of the globus pallidus on arm movements in monkeys. III. Timing of movement-related information. J Neurophysiol 54:433–448.

Arber S, Costa RM (2018) Connecting neuronal circuits for movement. Science 360:1403–1404.

Arkadir D, Morris G, Vaadia E, Bergman H (2004) Independent coding of movement direction and reward prediction by single pallidal neurons. J Neurosci 24:10047–10056.

Aron AR, Poldrack RA (2006) Cortical and subcortical contributions to Stop signal response inhibition: role of the subthalamic nucleus. J Neurosci 26:2424–2433.

Aron AR, Durston S, Eagle DM, Logan GD, Stinear CM, Stuphorn V (2007) Converging evidence for a fronto-basal-ganglia network for inhibitory control of action and cognition. J Neurosci 27:11860–11864.

Beal MF (2001) Experimental models of Parkinson's disease. Nat Rev Neurosci 2:325–334.

Bergman H, Wichmann T, DeLong MR (1990) Reversal of experimental parkinsonism by lesions of the subthalamic nucleus. Science 249:1436–1438.

Bergman H, Wichmann T, Karmon B, DeLong MR (1994) The primate subthalamic nucleus. II. Neuronal activity in the MPTP model of parkinsonism. J Neurophysiol 72:507–520.

Bergman H, Feingold A, Nini A, Raz A, Slovin H, Abeles M, Vaadia E (1998) Physiological aspects of information processing in the basal ganglia of normal and parkinsonian primates. Trends Neurosci 21:32–38.

Bernard V, Bolam JP (1998) Subcellular and subsynaptic distribution of the NR1 subunit of the NMDA receptor in the neostriatum and globus pallidus of the rat: co-localization at synapses with the GluR2/3 subunit of the AMPA receptor. Eur J Neurosci 10:3721–3736.

Betarbet R, Porter RH, Greenamyre JT (2000) GluR1 glutamate receptor subunit is regulated differentially in the primate basal ganglia following nigrostriatal dopamine denervation. J Neurochem 74:1166–1174.

Bevan MD, Booth PA, Eaton SA, Bolam JP (1998) Selective innervation of neostriatal interneurons by a subclass of neuron in the globus pallidus of the rat. J Neurosci 18:9438–9452.

Bevan MD, Magill PJ, Terman D, Bolam JP, Wilson CJ (2002) Move to the rhythm: oscillations in the subthalamic nucleus-external globus pallidus network. Trends Neurosci 25:525–531.

Bezard E, Przedborski S (2011) A tale on animal models of Parkinson's disease. Mov Disord 26:993–1002.

Bogacz R, Martin Moraud E, Abdi A, Magill PJ, Baufreton J (2016) Properties of neurons in external globus pallidus can support optimal action selection. PLoS Comput Biol 12:e1005004.

Boyden ES, Zhang F, Bamberg E, Nagel G, Deisseroth K (2005) Millisecond-timescale, genetically targeted optical control of neural activity. Nat Neurosci 8:1263–1268.

Brown P (2006) Bad oscillations in Parkinson's disease. J Neural Transm Suppl 6:27–30.

Carpenter MB, Baton RR 3rd, Carleton SC, Keller JT (1981a) Interconnections and organization of pallidal and subthalamic nucleus neurons in the monkey. J Comp Neurol 197:579–603.

Carpenter MB, Carleton SC, Keller JT, Conte P (1981b) Connections of the subthalamic nucleus in the monkey. Brain Res 224:1–29.

Chan CS, Glajch KE, Gertler TS, Guzman JN, Mercer JN, Lewis AS, Goldberg AB, Tkatch T, Shigemoto R, Fleming SM, Chetkovich DM, Osten P, Kita H, Surmeier DJ (2011) HCN channelopathy in external globus pallidus neurons in models of Parkinson's disease. Nat Neurosci 14:85–92.

Chan CS, Peterson JD, Gertler TS, Glajch KE, Quintana RE, Cui Q, Sebel LE, Plotkin JL, Shen W, Heiman M, Heintz N, Greengard P, Surmeier DJ (2012) Strain-specific regulation of striatal phenotype in Drd2-eGFP BAC transgenic mice. J Neurosci 32:9124–9132.

Cherian S, Cui Q, Pamukcu A, Chang IY, Berceau BL, Xenias H, Higgs MH, Rajamanickam S, Chen Y, Du X, Zhang Y, McMorrow H, Abecassis ZA, Boca SM, Justice NJ, Wilson CJ, Chan CS (2020) Dissociable roles of pallidal neuron subtypes in regulating motor patterns. bioRxiv. doi: https://doi.org/10.1101/2020.08.23.263053.

Chu HY, Atherton JF, Wokosin D, Surmeier DJ, Bevan MD (2015) Heterosynaptic regulation of external globus pallidus inputs to the subthalamic nucleus by the motor cortex. Neuron 85:364–376.

Clarke NP, Bolam JP (1998) Distribution of glutamate receptor subunits at neurochemically characterized synapses in the entopeduncular nucleus and subthalamic nucleus of the rat. J Comp Neurol 397:403–420.

Cox J, Witten IB (2019) Striatal circuits for reward learning and decision-making. Nat Rev Neurosci 20:482–494.

Cruz AV, Mallet N, Magill PJ, Brown P, Averbeck BB (2011) Effects of dopamine depletion on information flow between the subthalamic nucleus and external globus pallidus. J Neurophysiol 106:2012–2023.

Cui Q, Pitt JE, Pamukcu A, Poulin JF, Mabrouk OS, Fiske MP, Fan IB, Augustine EC, Young KA, Kennedy RT, Awatramani R, Chan CS (2016) Blunted mGluR activation disinhibits striatopallidal transmission in parkinsonian mice. Cell Rep 17:2431–2444.

Crompe B, Aristieta A, Leblois A, Elsherbiny S, Boraud T, Mallet NP (2020) The globus pallidus orchestrates abnormal network dynamics in a model of Parkinsonism. Nat Commun 11:1570.

Dauer W, Przedborski S (2003) Parkinson's disease: mechanisms and models. Neuron 39:889–909.

DeLong MR (1971) Activity of pallidal neurons during movement. J Neurophysiol 34:414–427.

DeLong MR (1990) Primate models of movement disorders of basal ganglia origin. Trends Neurosci 13:281–285.

DeLong MR, Wichmann T (2007) Circuits and circuit disorders of the basal ganglia. Arch Neurol 64:20–24.

DeLong MR, Wichmann T (2015) Basal ganglia circuits as targets for neuromodulation in Parkinson disease. JAMA Neurol 72:1354–1360.

DeLong MR, Crutcher MD, Georgopoulos AP (1985) Primate globus pallidus and subthalamic nucleus: functional organization. J Neurophysiol 53:530–543.

Deschênes M, Bourassa J, Doan VD, Parent A (1996) A single-cell study of the axonal projections arising from the posterior intralaminar thalamic nuclei in the rat. Eur J Neurosci 8:329–343.

Dodson PD, Larvin JT, Duffell JM, Garas FN, Doig NM, Kessaris N, Duguid IC, Bogacz R, Butt SJ, Magill PJ (2015) Distinct developmental origins manifest in the specialized encoding of movement by adult neurons of the external globus pallidus. Neuron 86:501–513.

Dudman JT, Krakauer JW (2016) The basal ganglia: from motor commands to the control of vigor. Curr Opin Neurobiol 37:158–166.

Durieux PF, Schiffmann SN, de Kerchove d'Exaerde A (2012) Differential regulation of motor control and response to dopaminergic drugs by D1R and D2R neurons in distinct dorsal striatum subregions. EMBO J 31:640–653.

Eagle DM, Baunez C, Hutcheson DM, Lehmann O, Shah AP, Robbins TW (2008) Stop-signal reaction-time task performance: role of prefrontal cortex and subthalamic nucleus. Cereb Cortex 18:178–188.

Fan KY, Baufreton J, Surmeier DJ, Chan CS, Bevan MD (2012) Proliferation of external globus pallidus-subthalamic nucleus synapses following degeneration of midbrain dopamine neurons. J Neurosci 32:13718–13728.

Fife KH, Gutierrez-Reed NA, Zell V, Bailly J, Lewis CM, Aron AR, Hnasko TS (2017) Causal role for the subthalamic nucleus in interrupting behavior. Elife 6:e27689.

Filion M, Tremblay L, Bédard PJ (1988) Abnormal influences of passive limb movement on the activity of globus pallidus neurons in parkinsonian monkeys. Brain Res 444:165–176.

Flandin P, Kimura S, Rubenstein JL (2010) The progenitor zone of the ventral medial ganglionic eminence requires Nkx2-1 to generate most of the globus pallidus but few neocortical interneurons. J Neurosci 30:2812–2823.

Freeze BS, Kravitz AV, Hammack N, Berke JD, Kreitzer AC (2013) Control of basal ganglia output by direct and indirect pathway projection neurons. J Neurosci 33:18531–18539.

Fujiyama F, Nakano T, Matsuda W, Furuta T, Udagawa J, Kaneko T (2016) A single-neuron tracing study of arkypallidal and prototypic neurons in healthy rats. Brain Struct Funct 221:4733–4740.

Gillies A, Willshaw D, Li Z (2002) Subthalamic-pallidal interactions are critical in determining normal and abnormal functioning of the basal ganglia. Proc Biol Sci 269:545–551.

Glajch KE, Kelver DA, Hegeman DJ, Cui Q, Xenias HS, Augustine EC, Hernández VM, Verma N, Huang TY, Luo M, Justice NJ, Chan CS (2016) Npas1$^+$ pallidal neurons target striatal projection neurons. J Neurosci 36:5472–5488.

Govorunova EG, Sineshchekov OA, Janz R, Liu X, Spudich JL (2015) Natural light-gated anion channels: a family of microbial rhodopsins for advanced optogenetics. Science 349:647–650.

Graybiel AM (2008) Habits, rituals, and the evaluative brain. Annu Rev Neurosci 31:359–387.

Gu BM, Schmidt R, Berke JD (2020) Globus pallidus dynamics reveal covert strategies for behavioral inhibition. Elife 9:e57215.

Hamani C, Saint-Cyr JA, Fraser J, Kaplitt M, Lozano AM (2004) The subthalamic nucleus in the context of movement disorders. Brain 127:4–20.

Hammond C, Yelnik J (1983) Intracellular labelling of rat subthalamic neurones with horseradish peroxidase: computer analysis of dendrites and characterization of axon arborization. Neuroscience 8:781–790.

Hammond C, Bergman H, Brown P (2007) Pathological synchronization in Parkinson's disease: networks, models and treatments. Trends Neurosci 30:357–364.

Hauber W, Lutz S, Münkle M (1998) The effects of globus pallidus lesions on dopamine-dependent motor behaviour in rats. Neuroscience 86:147–157.

Hegeman DJ, Hong ES, Hernández VM, Chan CS (2016) The external globus pallidus: progress and perspectives. Eur J Neurosci 43:1239–1265.

Hernández VM, Hegeman DJ, Cui Q, Kelver DA, Fiske MP, Glajch KE, Pitt JE, Huang TY, Justice NJ, Chan CS (2015) Parvalbumin$^+$ neurons and Npas1$^+$ neurons are distinct neuron classes in the mouse external globus pallidus. J Neurosci 35:11830–11847.

Ho J, Tumkaya T, Aryal S, Choi H, Claridge-Chang A (2019) Moving beyond P values: data analysis with estimation graphics. Nat Methods 16:565–566.

Holgado AJ, Terry JR, Bogacz R (2010) Conditions for the generation of beta oscillations in the subthalamic nucleus-globus pallidus network. J Neurosci 30:12340–12352.

Hunt AJ Jr, Dasgupta R, Rajamanickam S, Jiang Z, Beierlein M, Chan CS, Justice NJ (2018) Paraventricular hypothalamic and amygdalar CRF neurons synapse in the external globus pallidus. Brain Struct Funct 223:2685–2698.

Hurtado JM, Gray CM, Tamas LB, Sigvardt KA (1999) Dynamics of tremor-related oscillations in the human globus pallidus: a single case study. Proc Natl Acad Sci U S A 96:1674–1679.

Iancu R, Mohapel P, Brundin P, Paul G (2005) Behavioral characterization of a unilateral 6-OHDA-lesion model of Parkinson's disease in mice. Behav Brain Res 162:1–10.

Isoda M, Hikosaka O (2008) Role for subthalamic nucleus neurons in switching from automatic to controlled eye movement. J Neurosci 28:7209–7218.

Ito M, Doya K (2011) Multiple representations and algorithms for reinforcement learning in the cortico-basal ganglia circuit. Curr Opin Neurobiol 21:368–373.

Iwamuro H (2011) Electrophysiological evidences of organization of cortical motor information in the basal ganglia. J Mov Disord 4:8–12.

Jahanshahi M, Obeso I, Rothwell JC, Obeso JA (2015) A fronto-striato-subthalamic-pallidal network for goal-directed and habitual inhibition. Nat Rev Neurosci 16:719–732.

Joel D, Ayalon L, Tarrasch R, Veenman L, Feldon J, Weiner I (1998) Electrolytic lesion of globus pallidus ameliorates the behavioral and neurodegenerative effects of quinolinic acid lesion of the striatum: a potential novel treatment in a rat model of Huntington's disease. Brain Res 787:143–148.

Johnson MD, Zhang J, Ghosh D, McIntyre CC, Vitek JL (2012) Neural targets for relieving parkinsonian rigidity and bradykinesia with pallidal deep brain stimulation. J Neurophysiol 108:567–577.

Kaneda K, Tachibana Y, Imanishi M, Kita H, Shigemoto R, Nambu A, Takada M (2005) Down-regulation of metabotropic glutamate receptor 1alpha in globus pallidus and substantia nigra of parkinsonian monkeys. Eur J Neurosci 22:3241–3254.

Karube F, Takahashi S, Kobayashi K, Fujiyama F (2019) Motor cortex can directly drive the globus pallidus neurons in a projection neuron type-dependent manner in the rat. Elife 8:e49511.

Ketzef M, Silberberg G (2020) Differential synaptic input to external globus pallidus neuronal subpopulations *in vivo*. bioRxiv. doi: https://doi.org/10.1101/2020.02.27.967869.

Kimura M, Kato M, Shimazaki H, Watanabe K, Matsumoto N (1996) Neural information transferred from the putamen to the globus pallidus during learned movement in the monkey. J Neurophysiol 76:3771–3786.

Kincaid AE, Penney JB Jr, Young AB, Newman SW (1991) Evidence for a projection from the globus pallidus to the entopeduncular nucleus in the rat. Neurosci Lett 128:121–125.

Kita H (1992) Responses of globus pallidus neurons to cortical stimulation: intracellular study in the rat. Brain Res 589:84–90.

Kita H (1994) Parvalbumin-immunopositive neurons in rat globus pallidus: a light and electron microscopic study. Brain Res 657:31–41.

Kita H (2007) Globus pallidus external segment. Prog Brain Res 160:111–133.

Kita H, Kitai ST (1987) Efferent projections of the subthalamic nucleus in the rat: light and electron microscopic analysis with the PHA-L method. J Comp Neurol 260:435–452.

Kita H, Kitai ST (1991) Intracellular study of rat globus pallidus neurons: membrane properties and responses to neostriatal, subthalamic and nigral stimulation. Brain Res 564:296–305.

Kita H, Kitai ST (1994) The morphology of globus pallidus projection neurons in the rat: an intracellular staining study. Brain Res 636:308–319.

Kita H, Tokuno H, Nambu A (1999) Monkey globus pallidus external segment neurons projecting to the neostriatum. Neuroreport 10:1467–1472.

Kita H, Nambu A, Kaneda K, Tachibana Y, Takada M (2004) Role of ionotropic glutamatergic and GABAergic inputs on the firing activity of neurons in the external pallidum in awake monkeys. J Neurophysiol 92:3069–3084.

Klaus A, Martins GJ, Paixao VB, Zhou P, Paninski L, Costa RM (2017) The spatiotemporal organization of the striatum encodes action space. Neuron 95:1171–1180.e7.

Klaus A, Alves da Silva J, Costa RM (2019) What, if, and when to move: basal ganglia circuits and self-paced action initiation. Annu Rev Neurosci 42:459–483.

Konitsiotis S, Kafetzopoulos E, Anastasopoulos D, Blanchet PJ (1998) Opposite rotation induced by dopamine agonists in rats with unilateral lesions of the globus pallidus or substantia nigra. Behav Brain Res 92:77–83.

Koshimizu Y, Fujiyama F, Nakamura KC, Furuta T, Kaneko T (2013) Quantitative analysis of axon bouton distribution of subthalamic nucleus neurons in the rat by single neuron visualization with a viral vector. J Comp Neurol 521:2125–2146.

Kovaleski RF, Callahan JW, Chazalon M, Wokosin DL, Baufreton J, Bevan MD (2020) Dysregulation of external globus pallidus-subthalamic nucleus network dynamics in parkinsonian mice during cortical slow-wave activity and activation. J Physiol 598:1897–1927.

Kravitz AV, Freeze BS, Parker PR, Kay K, Thwin MT, Deisseroth K, Kreitzer AC (2010) Regulation of parkinsonian motor behaviours by optogenetic control of basal ganglia circuitry. Nature 466:622–626.

Krzywinski M, Altman N (2014) Visualizing samples with box plots. Nat Methods 11:119–120.

Kühn AA, Kupsch A, Schneider GH, Brown P (2006) Reduction in subthalamic 8-35 Hz oscillatory activity correlates with clinical improvement in Parkinson's disease. Eur J Neurosci 23:1956–1960.

Levy R, Lang AE, Dostrovsky JO, Pahapill P, Romas J, Saint-Cyr J, Hutchison WD, Lozano AM (2001) Lidocaine and muscimol microinjections in subthalamic nucleus reverse Parkinsonian symptoms. Brain 124:2105–2118.

Leys C, Ley C, Klein O, Bernard P, Licata L (2013) Detecting outliers: do not use standard deviation around the mean, use absolute deviation around the median. J Exp Soc Psychol 49:764–766.

Little S, Brown P (2014) The functional role of beta oscillations in Parkinson's disease. Parkinsonism Relat Disord 20 [Suppl 1]:S44–S48.

Mahn M, Gibor L, Patil P, Cohen-Kashi Malina K, Oring S, Printz Y, Levy R, Lampl I, Yizhar O (2018) High-efficiency optogenetic silencing with

soma-targeted anion-conducting channelrhodopsins. Nat Commun 9:4125.

Mallet N, Pogosyan A, Márton LF, Bolam JP, Brown P, Magill PJ (2008) Parkinsonian beta oscillations in the external globus pallidus and their relationship with subthalamic nucleus activity. J Neurosci 28:14245–14258.

Mallet N, Micklem BR, Henny P, Brown MT, Williams C, Bolam JP, Nakamura KC, Magill PJ (2012) Dichotomous organization of the external globus pallidus. Neuron 74:1075–1086.

Mallet N, Schmidt R, Leventhal D, Chen F, Am N, Boraud T, Berke JD (2016) Arkypallidal cells send a stop signal to striatum. Neuron 89:308–316.

Mastro KJ, Bouchard RS, Holt HA, Gittis AH (2014) Transgenic mouse lines subdivide external segment of the globus pallidus (GPe) neurons and reveal distinct GPe output pathways. J Neurosci 34:2087–2099.

Mastro KJ, Zitelli KT, Willard AM, Leblanc KH, Kravitz AV, Gittis AH (2017) Cell-specific pallidal intervention induces long-lasting motor recovery in dopamine-depleted mice. Nat Neurosci 20:815–823.

McGregor MM, Nelson AB (2019) Circuit mechanisms of Parkinson's disease. Neuron 101:1042–1056.

McIver EL, Atherton JF, Chu HY, Cosgrove KE, Kondapalli J, Wokosin D, Surmeier DJ, Bevan MD (2019) Maladaptive downregulation of autonomous subthalamic nucleus activity following the loss of midbrain dopamine neurons. Cell Rep 28:992–1002.e4.

Meredith GE, Kang UJ (2006) Behavioral models of Parkinson's disease in rodents: a new look at an old problem. Mov Disord 21:1595–1606.

Mink JW (1996) The basal ganglia: focused selection and inhibition of competing motor programs. Prog Neurobiol 50:381–425.

Mink JW (2018) Basal ganglia mechanisms in action selection, plasticity, and dystonia. Eur J Paediatr Neurol 22:225–229.

Mink JW, Thach WT (1987) Preferential relation of pallidal neurons to ballistic movements. Brain Res 417:393–398.

Mink JW, Thach WT (1991a) Basal ganglia motor control. II. Late pallidal timing relative to movement onset and inconsistent pallidal coding of movement parameters. J Neurophysiol 65:301–329.

Mink JW, Thach WT (1991b) Basal ganglia motor control. I. Nonexclusive relation of pallidal discharge to five movement modes. J Neurophysiol 65:273–300.

Mitchell SJ, Richardson RT, Baker FH, DeLong MR (1987) The primate globus pallidus: neuronal activity related to direction of movement. Exp Brain Res 68:491–505.

Mouroux M, Hassani OK, Féger J (1997) Electrophysiological and Fos immunohistochemical evidence for the excitatory nature of the parafascicular projection to the globus pallidus. Neuroscience 81:387–397.

Mullie Y, Arto I, Yahiaoui N, Drew T (2020) Contribution of the entopeduncular nucleus and the globus pallidus to the control of locomotion and visually guided gait modifications in the cat. Cereb Cortex 30:5121–5146.

Mushiake H, Strick PL (1995) Pallidal neuron activity during sequential arm movements. J Neurophysiol 74:2754–2758.

Naito A, Kita H (1994) The cortico-pallidal projection in the rat: an anterograde tracing study with biotinylated dextran amine. Brain Res 653:251–257.

Nambu A (2011) Somatotopic organization of the primate basal ganglia. Front Neuroanat 5:26.

Nambu A, Llinás R (1997) Morphology of globus pallidus neurons: its correlation with electrophysiology in guinea pig brain slices. J Comp Neurol 377:85–94.

Nambu A, Tachibana Y (2014) Mechanism of parkinsonian neuronal oscillations in the primate basal ganglia: some considerations based on our recent work. Front Syst Neurosci 8:74.

Nambu A, Yoshida S, Jinnai K (1990) Discharge patterns of pallidal neurons with input from various cortical areas during movement in the monkey. Brain Res 519:183–191.

Nambu A, Tokuno H, Hamada I, Kita H, Imanishi M, Akazawa T, Ikeuchi Y, Hasegawa N (2000) Excitatory cortical inputs to pallidal neurons via the subthalamic nucleus in the monkey. J Neurophysiol 84:289–300.

Nóbrega-Pereira S, Gelman D, Bartolini G, Pla R, Pierani A, Marín O (2010) Origin and molecular specification of globus pallidus neurons. J Neurosci 30:2824–2834.

Norton S (1976) Hyperactive behavior of rats after lesions of the globus pallidus. Brain Res Bull 1:193–202.

Nuzzo RL (2016) The box plots alternative for visualizing quantitative data. PM R 8:268–272.

Obeso JA, Rodríguez-Oroz MC, Rodríguez M, Lanciego JL, Artieda J, Gonzalo N, Olanow CW (2000) Pathophysiology of the basal ganglia in Parkinson's disease. Trends Neurosci 23:S8–S19.

Oh YM, Karube F, Takahashi S, Kobayashi K, Takada M, Uchigashima M, Watanabe M, Nishizawa K, Kobayashi K, Fujiyama F (2017) Using a novel PV-Cre rat model to characterize pallidonigral cells and their terminations. Brain Struct Funct 222:2359–2378.

Ossowska K, S̈miałowska M, Wolfarth S (1983) A biphasic influence of globus pallidus lesions: spontaneous catalepsy followed by anticataleptic effect. Pharmacol Biochem Behav 19:169–176.

Owen SF, Liu MH, Kreitzer AC (2019) Thermal constraints on in vivo optogenetic manipulations. Nat Neurosci 22:1061–1065.

Papathanou M, Björklund ÅK, Martis-Thiele MM, Wallén-Mackenzie Å (2019) Single-nuclei transcriptomic analysis of the subthalamic nucleus reveals different Pitx2-positive subpopulations. Commun Biol 3:338.

Parent A, Smith Y (1987) Organization of efferent projections of the subthalamic nucleus in the squirrel monkey as revealed by retrograde labeling methods. Brain Res 436:296–310.

Parent A, Hazrati LN (1995) Functional anatomy of the basal ganglia. II. The place of subthalamic nucleus and external pallidum in basal ganglia circuitry. Brain Res Brain Res Rev 20:128–154.

Patel AB, Hays SA, Bureau I, Huber KM, Gibson JR (2013) A target cell-specific role for presynaptic Fmr1 in regulating glutamate release onto neocortical fast-spiking inhibitory neurons. J Neurosci 33:2593–2604.

Pennartz CM, Berke JD, Graybiel AM, Ito R, Lansink CS, van der Meer M, Redish AD, Smith KS, Voorn P (2009) Corticostriatal interactions during learning, memory processing, and decision making. J Neurosci 29:12831–12838.

Plenz D, Kital ST (1999) A basal ganglia pacemaker formed by the subthalamic nucleus and external globus pallidus. Nature 400:677–682.

Porter RH, Greene JG, Higgins DS Jr, Greenamyre JT (1994) Polysynaptic regulation of glutamate receptors and mitochondrial enzyme activities in the basal ganglia of rats with unilateral dopamine depletion. J Neurosci 14:7192–7199.

Redgrave P, Rodriguez M, Smith Y, Rodriguez-Oroz MC, Lehericy S, Bergman H, Agid Y, DeLong MR, Obeso JA (2010) Goal-directed and habitual control in the basal ganglia: implications for Parkinson's disease. Nat Rev Neurosci 11:760–772.

Sadikot AF, Parent A, Smith Y, Bolam JP (1992) Efferent connections of the centromedian and parafascicular thalamic nuclei in the squirrel monkey: a light and electron microscopic study of the thalamostriatal projection in relation to striatal heterogeneity. J Comp Neurol 320:228–242.

Sato F, Lavallée P, Lévesque M, Parent A (2000a) Single-axon tracing study of neurons of the external segment of the globus pallidus in primate. J Comp Neurol 417:17–31.

Sato F, Parent M, Levesque M, Parent A (2000b) Axonal branching pattern of neurons of the subthalamic nucleus in primates. J Comp Neurol 424:142–152.

Saunders A, Oldenburg IA, Berezovskii VK, Johnson CA, Kingery ND, Elliott HL, Xie T, Gerfen CR, Sabatini BL (2015) A direct GABAergic output from the basal ganglia to frontal cortex. Nature 521:85–89.

Saunders A, Huang KW, Sabatini BL (2016) Globus pallidus externus neurons expressing parvalbumin interconnect the subthalamic nucleus and striatal interneurons. PLoS One 11:e0149798.

Saunders A, Macosko EZ, Wysoker A, Goldman M, Krienen FM, de Rivera H, Bien E, Baum M, Bortolin L, Wang S, Goeva A, Nemesh J, Kamitaki N, Brumbaugh S, Kulp D, McCarroll SA (2018) Molecular Diversity and Specializations among the Cells of the Adult Mouse Brain. Cell 174:1015–1030.e16.

Schallert T, Fleming SM, Leasure JL, Tillerson JL, Bland ST (2000) CNS plasticity and assessment of forelimb sensorimotor outcome in unilateral rat models of stroke, cortical ablation, parkinsonism and spinal cord injury. Neuropharmacology 39:777–787.

Schindelin J, Arganda-Carreras I, Frise E, Kaynig V, Longair M, Pietzsch T, Preibisch S, Rueden C, Saalfeld S, Schmid B, Tinevez JY, White DJ, Hartenstein V, Eliceiri K, Tomancak P, Cardona A (2012) Fiji: an open-source platform for biological-image analysis. Nat Methods 9:676–682.

Schmidt R, Leventhal DK, Mallet N, Chen F, Berke JD (2013) Canceling actions involves a race between basal ganglia pathways. Nat Neurosci 16:1118–1124.

Schneider JS, Olazabal UE (1984) Behaviorally specific limb use deficits following globus pallidus lesions in rats. Brain Res 308:341–346.

Schweizer N, Pupe S, Arvidsson E, Nordenankar K, Smith-Anttila CJA, Mahmoudi S, Andrén A, Dumas S, Rajagopalan A, Lévesque D, Leão RN, Wallén-Mackenzie Å (2014) Limiting glutamate transmission in a Vglut2-expressing subpopulation of the subthalamic nucleus is sufficient to cause hyperlocomotion. Proc Natl Acad Sci U S A 111:7837–7842.

Sharott A, Gulberti A, Zittel S, Tudor Jones AA, Fickel U, Münchau A, Köppen JA, Gerloff C, Westphal M, Buhmann C, Hamel W, Engel AK, Moll CK (2014) Activity parameters of subthalamic nucleus neurons selectively predict motor symptom severity in Parkinson's disease. J Neurosci 34:6273–6285.

Shigemoto R, Kulik A, Roberts JD, Ohishi H, Nusser Z, Kaneko T, Somogyi P (1996) Target-cell-specific concentration of a metabotropic glutamate receptor in the presynaptic active zone. Nature 381:523–525.

Shin S, Sommer MA (2010) Activity of neurons in monkey globus pallidus during oculomotor behavior compared with that in substantia nigra pars reticulata. J Neurophysiol 103:1874–1887.

Smith Y, Bolam JP, Von Krosigk M (1990a) Topographical and synaptic organization of the GABA-containing pallidosubthalamic projection in the rat. Eur J Neurosci 2:500–511.

Smith Y, Hazrati LN, Parent A (1990b) Efferent projections of the subthalamic nucleus in the squirrel monkey as studied by the PHA-L anterograde tracing method. J Comp Neurol 294:306–323.

Smith Y, Bevan MD, Shink E, Bolam JP (1998) Microcircuitry of the direct and indirect pathways of the basal ganglia. Neuroscience 86:353–387.

Soares J, Kliem MA, Betarbet R, Greenamyre JT, Yamamoto B, Wichmann T (2004) Role of external pallidal segment in primate parkinsonism: comparison of the effects of 1-methyl-4-phenyl-1,2,3,6-tetrahydropyridine-induced parkinsonism and lesions of the external pallidal segment. J Neurosci 24:6417–6426.

Streit M, Gehlenborg N (2014) Bar charts and box plots. Nat Methods 11:117.

Sun HY, Li Q, Bartley AF, Dobrunz LE (2018) Target-cell-specific short-term plasticity reduces the excitatory drive onto ca1 interneurons relative to pyramidal cells during physiologically-derived spike trains. Neuroscience 388:430–447.

Suryanarayana SM, Hellgren Kotaleski J, Grillner S, Gurney KN (2019) Roles for globus pallidus externa revealed in a computational model of action selection in the basal ganglia. Neural Netw 109:113–136.

Svoboda K (2019) Using rabies virus for tracing neural connections: caveats and limitations exposed by studies of barrel cortex circuits. Available at https://spikesphotons.blog/.

Tachibana Y, Iwamuro H, Kita H, Takada M, Nambu A (2011) Subthalamopallidal interactions underlying parkinsonian neuronal oscillations in the primate basal ganglia. Eur J Neurosci 34:1470–1484.

Terman D, Rubin JE, Yew AC, Wilson CJ (2002) Activity patterns in a model for the subthalamopallidal network of the basal ganglia. J Neurosci 22:2963–2976.

Tervo DG, Hwang BY, Viswanathan S, Gaj T, Lavzin M, Ritola KD, Lindo S, Michael S, Kuleshova E, Ojala D, Huang CC, Gerfen CR, Schiller J, Dudman JT, Hantman AW, Looger LL, Schaffer DV, Karpova AY (2016) A designer AAV variant permits efficient retrograde access to projection neurons. Neuron 92:372–382.

Ungerstedt U (1968) 6-Hydroxy-dopamine induced degeneration of central monoamine neurons. Eur J Pharmacol 5:107–110.

Vitek JL, Hashimoto T, Peoples J, DeLong MR, Bakay RA (2004) Acute stimulation in the external segment of the globus pallidus improves parkinsonian motor signs. Mov Disord 19:907–915.

Vitek JL, Zhang J, Hashimoto T, Russo GS, Baker KB (2012) External pallidal stimulation improves parkinsonian motor signs and modulates neuronal activity throughout the basal ganglia thalamic network. Exp Neurol 233:581–586.

Walters JR, Hu D, Itoga CA, Parr-Brownlie LC, Bergstrom DA (2007) Phase relationships support a role for coordinated activity in the indirect pathway in organizing slow oscillations in basal ganglia output after loss of dopamine. Neuroscience 144:762–776.

Wessel JR, Aron AR (2017) On the globality of motor suppression: unexpected events and their influence on behavior and cognition. Neuron 93:259–280.

Wichmann T, DeLong MR (1996) Functional and pathophysiological models of the basal ganglia. Curr Opin Neurobiol 6:751–758.

Wichmann T, DeLong MR, Guridi J, Obeso JA (2011) Milestones in research on the pathophysiology of Parkinson's disease. Mov Disord 26:1032–1041.

Wilson CJ (2013) Active decorrelation in the basal ganglia. Neuroscience 250:467–482.

Xiao C, Miwa JM, Henderson BJ, Wang Y, Deshpande P, McKinney SL, Lester HA (2015) Nicotinic receptor subtype-selective circuit patterns in the subthalamic nucleus. J Neurosci 35:3734–3746.

Yasukawa T, Kita T, Xue Y, Kita H (2004) Rat intralaminar thalamic nuclei projections to the globus pallidus: a biotinylated dextran amine anterograde tracing study. J Comp Neurol 471:153–167.

Yelnik J, Percheron G (1979) Subthalamic neurons in primates: a quantitative and comparative analysis. Neuroscience 4:1717–1743.

Yoon HH, Park JH, Kim YH, Min J, Hwang E, Lee CJ, Suh JK, Hwang O, Jeon SR (2014) Optogenetic inactivation of the subthalamic nucleus improves forelimb akinesia in a rat model of Parkinson disease. Neurosurgery 74:533–540.

Yoshida A, Tanaka M (2016) Two types of neurons in the primate globus pallidus external segment play distinct roles in antisaccade generation. Cereb Cortex 26:1187–1199.

Zaidel A, Arkadir D, Israel Z, Bergman H (2009) Akineto-rigid vs. tremor syndromes in Parkinsonism. Curr Opin Neurol 22:387–393.